

Article

# Normal Operating Performance Study of 15 MW Floating Wind Turbine System Using Semisubmersible Taida Floating Platform in Hsinchu Offshore Area

Hoi-Yi Tong, Tsung-Yueh Lin  and Shiu-Wu Chau \* 

The Department of Engineering Science and Ocean Engineering, National Taiwan University,  
Taipei 10617, Taiwan

\* Correspondence: chausw@ntu.edu.tw

**Abstract:** This study predicted the motion response and power performance of a floating wind turbine system equipped with a semisubmersible Taida platform, an IEA 15 MW wind turbine, and a  $3 \times 2$  mooring design in the Hsinchu offshore area in the Taiwan Strait. The hydrodynamic properties were calculated using ANSYS-AQWA and STAR-CCM+. The motion equations were solved by OrcaFlex to obtain the motion response and generator power, as well as the dynamics of the mooring system and aerodynamics of the wind turbine. The waves were assumed to share the same direction as the wind. This study compared the mean values and standard deviations of the motion response, generator power, and mooring line tension between the potential- and viscous-flow approaches by considering the combination of seven wind directions and four current directions under two wave conditions in the Hsinchu offshore area. The numerical prediction shows that the viscous effect has a larger impact on the hydrodynamic properties in the heave, roll, and pitch motions. The angle between the leading mooring line of the system and dominant wind direction in the Taiwan Strait, which comes from the northeast, should be from  $120^\circ$  to  $180^\circ$  in order to deliver a relatively favorable performance of the system.



**Citation:** Tong, H.-Y.; Lin, T.-Y.; Chau, S.-W. Normal Operating Performance Study of 15 MW Floating Wind Turbine System Using Semisubmersible Taida Floating Platform in Hsinchu Offshore Area. *J. Mar. Sci. Eng.* **2023**, *11*, 457. <https://doi.org/10.3390/jmse11020457>

Academic Editors:  
Unai Fernandez-Gamiz, Giuseppe Roberto Tomasicchio and Eva LOUKOGEORAKI

Received: 14 December 2022  
Revised: 13 February 2023  
Accepted: 14 February 2023  
Published: 20 February 2023



**Copyright:** © 2023 by the authors. Licensee MDPI, Basel, Switzerland. This article is an open access article distributed under the terms and conditions of the Creative Commons Attribution (CC BY) license (<https://creativecommons.org/licenses/by/4.0/>).

**Keywords:** floating wind turbine; semisubmersible; hydrodynamic properties; operating performance; Hsinchu offshore area; Taiwan Strait

## 1. Introduction

In April 2022, the Global Wind Energy Council (GWEC) reported that more than 93.6 GW of onshore and offshore wind energy capacity was newly installed in 2021, and that the total amount of the global wind energy capacity has exceeded 837 GW, which is the second highest record over the years [1]. The development of green energy, and especially wind power, is one of the most important global issues of the future. The government of Taiwan aims to install an offshore wind energy capacity of 20 GW by 2035 [2]. Having high wind power potential, the Taiwan Strait is a promising site for developing offshore wind turbines, and especially in the area where the water depth exceeds 50 m [3]. When an increasing water depth heavily challenges the cost and installation of bottom-fixed offshore wind turbines, floating wind turbines are a relatively economical solution in deep waters. Thus, research on the motion response and generator power of floating offshore wind turbines is an important task to efficiently explore the offshore wind energy in the Taiwan Strait.

Previous studies on the offshore wind resources and environment conditions of the Taiwan Strait are first summarized. The seismic and geological data of the Zhangbin offshore area were analyzed in [4], and the influence of climate change on the wind resources in the Taiwan Strait was predicted in [5]. The performances of different types of floating platforms have also been investigated in related research. The various design concepts for floating offshore platforms are commonly categorized into four basic types:

spar, semisubmersible, barge, and tension leg platforms [6]. The motion response of spar-type platforms was studied in [7–9]. References [10,11] investigated the motion response of semisubmersible platforms. Li, et al. [12] compared the hydrodynamic and global motion behavior in the South China Sea among semisubmersible, tension leg, and spar-type platforms. According to [12], the spar-type platform has a better performance in general, but it requires a deep-water depth. De Guzman, et al. [13] proposed a reduced-draft-spar concept with high stability for shallow-water regions. In contrast, the performance of the semisubmersible platform is promising because it only requires a relatively shallow water depth, which is suitable for the area with of the Taiwan Strait with high wind power potential, where the water depth ranges from 50 m to 70 m. For semisubmersible platforms, pontoons and columns provide resistance to aerodynamic loads, and braces and trusses deliver resistance to hydrodynamic loads. However, the complex construction of the tower systems, either at-center or off-center [14], might involve issues of structural fatigue. Moreover, the early research on the performances of floating offshore wind turbines mainly focused on the NREL 5 MW [15] and DTU 10 MW [16] wind turbines. The current tendency for offshore wind turbines is designs with increasing rotor sizes. For example, Liu and Manuel [17] developed the mooring systems for a 13.2 MW wind turbine. IEA 15 MW offshore wind turbines [18] are rarely employed in the related studies for the Taiwan Strait. Therefore, the performance of a wind turbine system equipped with an IEA 15 MW wind turbine under the metocean conditions of the Hsinchu offshore area, which is one of the sites with the most potential in the Taiwan Strait, requires further study.

Studies in the field of floating offshore wind turbines have adopted various approaches. Udoh and Zou [19] used coupled OrcaFlex and FAST simulation to study the motion response of the DTU 10 MW mounted on various platforms. Zhang, et al. [20,21] solved the viscous-flow field of the OC5 DeepCwind semisubmersible platform with an NREL 5 MW wind turbine. Because the viscous-flow calculation generally requires tremendous computational resources, it is not efficient for the transit analysis of irregular waves. Instead of using time-consuming viscous-flow calculations, the authors of [22] computed the hydrodynamic coefficients via the boundary element method based on the potential-flow theory. Luquet, et al. [23] solved viscous-flow fields via the explicit spectrum method to investigate the nonlinear free-surface effect of a tension leg platform. Sethuraman and Venugopal [24] conducted a seakeeping experiment of a ballasted floater with a 2 MW wind turbine and compared it with OrcaFlex numerical results. Reference [25] analyzed the motion response of a 5 MW wind turbine on a semisubmersible platform, and they found that the bottom plates on the pontoon had significant effects in reducing the wind-induced rolling. Nematbakhsh, et al. [26] developed a viscous-flow code to study the performance degradation of a floating 5 MW wind turbine in extreme sea states in the North Sea. The study concluded that the nonlinear interaction between the floater and free surface could not be described by the potential-flow theory. Reference [27] used OpenFOAM to simulate the motion response of a moored floater, and they validated the numerical results against experiments. Karimirad and Michailides [28] coupled several types of software, including HydroD, GeniE, WAMIT, SIMA, Simo-Riflex, and Simo-Riflex-Aerodyn, to analyze a 5 MW wind turbine on a semisubmersible platform under normal and extreme conditions. The study found that oblique wave loads contributed to the yaw motion. Zheng and Lei [29] analyzed a floating offshore wind turbine integrated with a steel fish farming cage by coupling FAST and WAMIT, and they found that its design is more resistant to overturning, heaving, pitching, and surging than OC3Hywinde3 and OC4DeepCwind. Ishihara and Zhang [30] used ANSYS-AQWA with the corrected Morison equation to study the motion response under irregular waves. The numerical results were then compared with the model test measurements. Lerch, et al. [31] considered three main degrees of freedom in FOWAT, FAST, and MATLAB to compute a 5 MW floating wind turbine in the European offshore regions, where the expected power capacity factor can reach 75%. Reference [32] used WADAM, which is a frequency-domain potential-flow solver, to simulate a moored 5 MW floating wind turbine with a water depth between 50 m and 70 m. The horizontal load in

the mooring lines was dominated by the wave load, while the axial tension was determined by the residual buoyancy. Ferrandis, et al. [33] compared the potential-flow-based and viscous-flow-based solvers AQWA, AEGIR, and STARCCM+, in the aspects of the viscosity and nonlinearities in the motions of a semisubmersible platform. When the frequency of the incident wave is closed to the natural frequency of the floater, the viscous solver can better describe the motions.

To lower the production cost, and to adapt the floating offshore wind turbine system to the metocean conditions in the Taiwan Strait, designing an indigenous floating offshore wind turbine is an essential task for Taiwan. The Taida floating platform [34] is an original delta-shaped semisubmersible platform designed by a research team at National Taiwan University. The proposal contains a new design shape for the floater, which is capable of delivering significant viscous damping to stabilize the motion in waves. The motion-induced viscous damping here is specifically addressed through the viscous-flow approach. This study predicted the motion response, generator power, and mooring line tension of a 15 MW floating wind turbine system equipped with a Taida platform, an IEA 15 MW offshore wind turbine, and a  $3 \times 2$  mooring design under the metocean conditions in the Hsinchu offshore area in the Taiwan Strait. Several aspects of viscous damping via comparison with the potential-flow approach are the second highlight of this study. According to [35], the local wind in the Taiwan Strait most likely comes from the northeast, with a probability of about 70%. The third highlight of this study is its aim to find the orientation range of the Taida platform with respect to the dominant wind direction, where the motion response and power output are the most favorable under the conditions of normal operation.

The present study is written in the following structure. Section 2 describes the Taida platform design. Section 3 describes the numerical framework and each submodule applied in the simulation. Section 4 discusses the motion response, power output, and mooring lines. Detailed comparisons between normal and high waves and between the potential-flow and viscous-flow modeling are included. Section 5 concludes the research.

## 2. Wind Turbine System Design

### 2.1. Floating Platform Design

The Taida platform, which was designed to carry a 15 MW wind turbine, was considered the target platform in this study. According to the design constrains of a 15 MW wind turbine system given in [34,36], the characteristic length of the Taida platform is limited to 85 m to fit in the drydock of a potential shipyard in Taiwan for production, and the wind turbine system is limited to a pitch angle between  $-10^\circ$  and  $10^\circ$  and a mean pitch angle between  $-5^\circ$  and  $5^\circ$  during normal operation.

The Taida platform is a three-column delta-shaped semisubmersible floating platform with a characteristic length of 81.6 m, height of 35 m, and draft of 20 m. The column under the turbine is 60% wider than the other two columns with the same size. The total displacement of the system is 23.683 kton. The specifications and dimensions of the Taida platform are shown in Table 1 and Figure 1, respectively.

**Table 1.** Specifications of Taida platform.

Properties (Unit)	Value	
Draft (m)	20	
Total System Displacement (kton)	23.683	
Total System CG (m)	(4.117, 0, -2.29)	
Principal Inertias about CG (kg·m <sup>2</sup> )	$I_{xx}$	$4.932 \times 10^{10}$
	$I_{yy}$	$5.335 \times 10^{10}$
	$I_{zz}$	$2.834 \times 10^{10}$
	$I_{xy}$	$-6.734 \times 10^5$
	$I_{xz}$	$-9.954 \times 10^9$
	$I_{yz}$	$-3.047 \times 10^6$

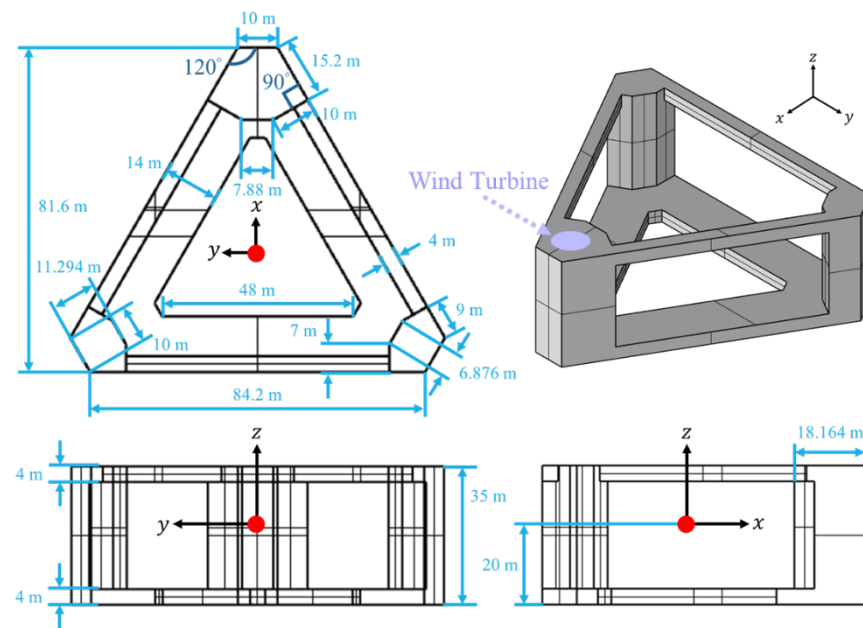


**Figure 1.** Dimensions of Taida platform.

### 2.2. Mooring Design

A  $3 \times 2$  mooring design was employed in this study. The mooring line was designed with the following constraints [37]: the allowable offset of the wind turbine system was 30% of the water depth, which was 21 m, to protect the dynamic cables, the anchor weight was preferably less than 18 tons, and the mooring chain was limited to a diameter of 16.51 cm.

Table 2 shows the specifications of the mooring lines. The Taida platform is equipped with two mooring lines on each column, and the angle between these two mooring lines is  $10^\circ$ , as shown in Figure 2. The fairleads are 18 m below the free surface. The water depth is assumed to be 70 m. The length of an unstretched mooring line is 448 m. The break load of the mooring line is 14.96 MN.

**Table 2.** Specifications of mooring lines.

Properties (Unit)	Value
Number of Mooring Lines	$3 \times 2$
Angle between Adjacent Lines ( $^\circ$ )	10/119.8
Depth to Anchors below SWL (m)	70
Depth to Fairleads below SWL (m)	18
Radius Measured from Centroid of Platform to Anchors (m)	484.3
Radius Measured from Centroid of Platform to Fairleads (m)	47.1
Unstretched Mooring Line Length (m)	448
Mooring Line Diameter (m)	0.229
Mooring Nominal Diameter (m)	0.127
Mooring Line Mass Density (kg/m)	321
Mooring Line Break Load (MN)	14.96
Mooring Line Axial Stiffness (GN)	1.377

### 2.3. Wind Turbine Design

An IEA 15 MW offshore wind turbine was employed in this study. The detailed design is given in [18,38]. The specifications and dimensions of the IEA 15 MW wind turbine are shown in Table 3 and Figure 3, respectively. It is an upwind wind turbine with three blades. The cut-in, rated, and cut-out wind speeds are 3 m/s, 10.59 m/s, and 25 m/s, respectively. The cut-in and rated rotor speeds are 5 RPM and 7.56 RPM, respectively. The hub height and rotor diameter are 150 m and 240 m, respectively. The DTU FFA-W3 airfoil series was used in the blade design of the IEA 15 MW offshore wind turbine. Figure 4 shows the

dependence of the blade pitch angle ( $\beta_b$ ), generator power ( $P_g$ ), rotor speed ( $\Omega_r$ ), and rotor thrust force ( $T_r$ ) on the wind speed at hub height ( $U_w$ ).

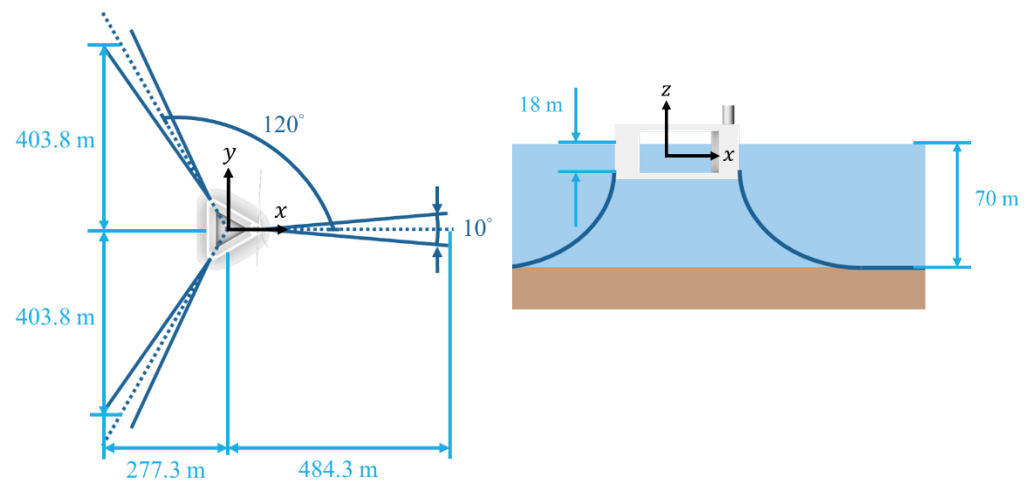


Figure 2. Mooring design of wind turbine system.

Table 3. Specifications of IEA 15 MW offshore wind turbine.

Properties (Unit)	Value
Rated Power (MW)	15
Blade Length (m)	120
Hub Height (m)	150
Hub/Rotor Diameters (m)	7.94/240
Tower Base Diameter (m)	10
Hub Overhang (m)	11.35
Cut-in/Rated/Cut-out Wind Speeds (m/s)	3/10.59/25
Cut-in/Rated Rotor Speeds (RPM)	5/7.56
Shaft Tilt/Precone Angles ( $^{\circ}$ )	6/4
Rotor Nacelle Assembly Mass (ton)	1016.6
Tower Mass (ton)	860

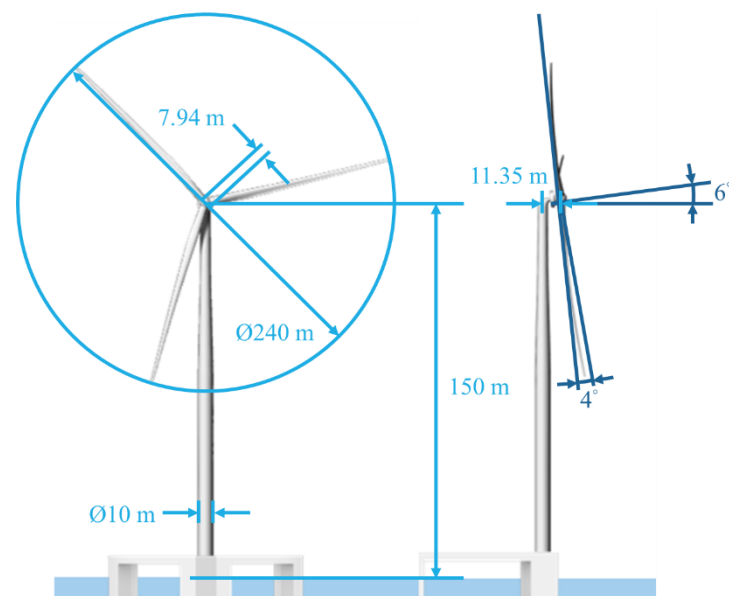
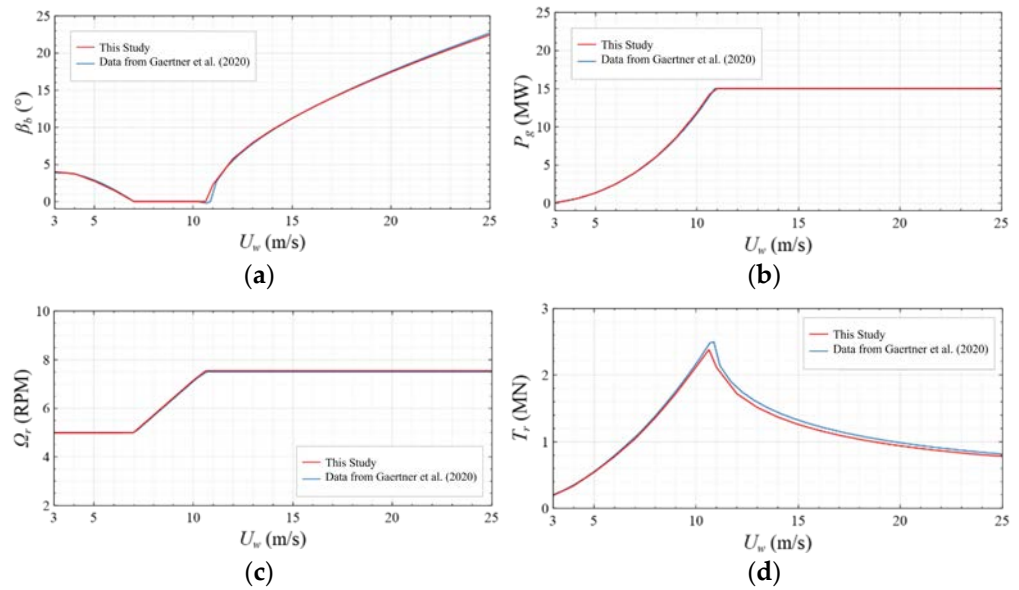


Figure 3. Dimensions of IEA 15 MW offshore wind turbine.



**Figure 4.** Comparison of (a) blade pitch angle, (b) generator power, (c) rotor speed, and (d) rotor thrust force between this study and [18].

### 3. Numerical Methods

A numerical framework for predicting the motion response and power performance of a floating wind turbine system is proposed in this study (Figure 5), in which the metocean condition of the Hsinchu offshore area is referenced from [35,39]. The hydrodynamic properties were predicted using ANSYS-AQWA via the potential-flow approach. The forced motion of the platform was simulated using STAR-CCM+ to obtain the hydrodynamic properties considering the viscous effects. The aerodynamics and dynamics of the mooring system were calculated using OrcaFlex via the blade element momentum theory and finite element method. With all these results, the equations of the motions were solved, and the motion response and generator power of the wind turbine system were obtained.

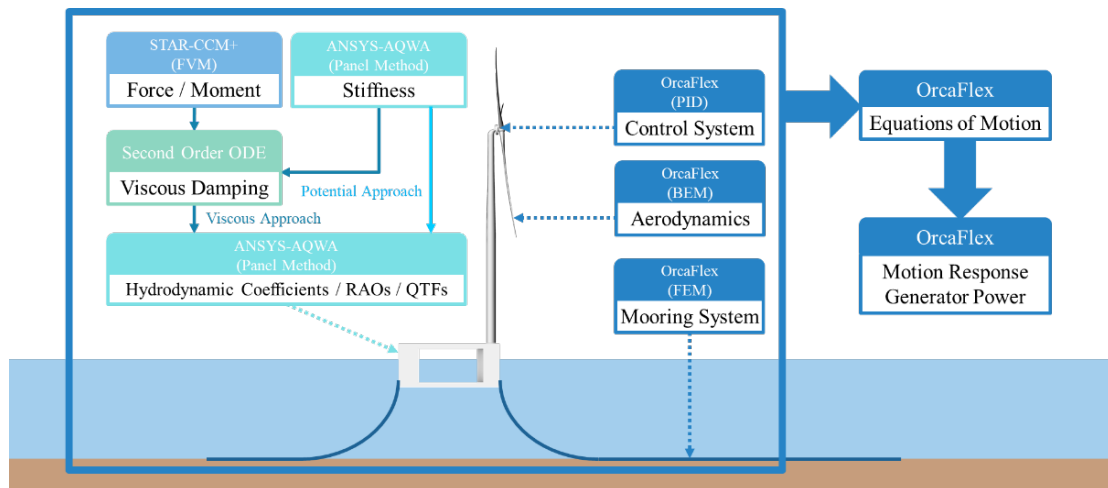


**Figure 5.** Numerical framework for floating wind turbine performance prediction.

Figure 5 shows the numerical framework for predicting the motion response and power performance of a floating wind turbine system. The numerical details of ANSYS-AQWA for the potential-flow hydrodynamic coefficients, STAR-CCM+ for the viscous damping, and OrcaFlex for the aerodynamics of the wind turbine, mooring, and motion, are elaborated in the following sections. The proposed framework was benchmarked with the

National Renewable Energy Laboratory (NREL)’s OC4 DeepCwind with a 5 MW wind turbine [10]. The results of the motions, rotor speed, pitch angle, and power generation agreed with the NREL reports [40] and thus confirmed that the proposed numerical framework is reliable. In addition, Hong [11] successfully predicted the performance of a disk-type semisubmersible floating wind turbine system installed in the Taiwan Strait. The same framework was also adopted in this study.

### 3.1. Equations of Motion

To predict the motion response and power performance of the floating wind turbine system, the motion equations with coupled effects were solved in OrcaFlex. The equation of the motion of the floating body is given as follows:

$$\sum_{j=1}^6 (M_{ij} + A_{ij})x_j'' + B_{ij}x_j' + C_{ij}x_j = F_i + F_i^o, \tag{1}$$

where  $M_{ij}$  is the body mass;  $A_{ij}$  is the added mass;  $B_{ij}$  is the damping;  $C_{ij}$  is the stiffness of the floating body;  $x_j$  is the displacement;  $x_j'$  is the velocity;  $x_j''$  is the acceleration. The subscripts ( $i, j = 1, 2, \dots, 6$ ) refer to the six degrees of freedom (i.e., surge, sway, heave, roll, pitch, and yaw), respectively. On the right-hand side of the equations,  $F_i$  is the wave-exciting force, and  $F_i^o$  is the force other than the fluid force, such as the aerodynamic loading and mooring tension.  $A_{ij}$ ,  $B_{ij}$ ,  $C_{ij}$ , and  $F_i$  come from the results of ANSYS-AQWA, as well as from the viscous damping prediction. The wave drift force, which is a kind of second-order force, is considered, while the motion response is solved in the time domain. The predicted viscous components are used in AQWA to obtain the response amplitude operators (RAOs).

As shown in Figure 6, the fluid force, which is divided into hydrodynamic force and hydrostatic force, is composed of  $A_{ij}x_j''$ ,  $B_{ij}x_j'$ ,  $C_{ij}x_j$ , and  $F_i$ . The hydrodynamic force is further divided into the wave-exciting force and radiation force. The former, which is a combination of the Froude–Krylov force and diffraction force, is provided by incoming waves under the condition that the floating body is fixed, while the latter, which is a combination of the added inertia force and damping force, is caused by the forced motion of the floating body without considering incoming waves. The Froude–Krylov force on the floating body is introduced by the unsteady pressure field generated by undisturbed waves, while the diffraction force is due to the disturbance of the floating body to the incoming waves.

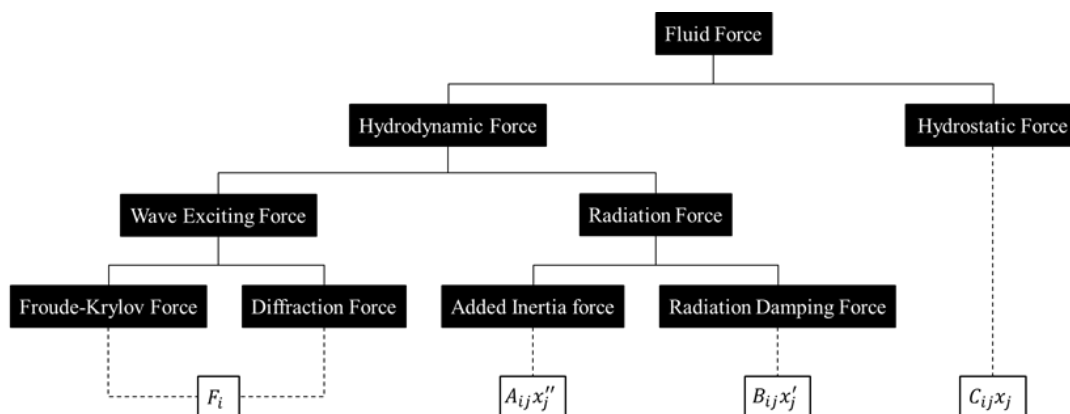


Figure 6. Components of fluid force.

### 3.2. Potential-Flow Modeling

Under the assumption of linear and small-amplitude waves, the hydrodynamic properties of the floating body were predicted in ANSYS-AQWA via the panel method, which is based on the three-dimensional potential-flow theory [41]. The flow field was assumed

to be inviscid, irrotational, and incompressible in the potential flow. The added mass and damping were obtained from the radiation force ( $F_r$ ):

$$F_r = \iint_S \sum_{j=1}^6 i\omega x_j \Phi_j(x, y, z) e^{-i\omega t} \mathbf{n}_i(x, y, z) dS = \sum_{j=1}^6 A_{ij} x_j'' + B_{ij} x_j', \quad (2)$$

where  $\Phi_j(x, y, z)$  is the radiation velocity potential;  $\omega$  is the angular frequency of the wave;  $x_j$  is the motion amplitude of the floating body;  $t$  is the time;  $\mathbf{n}_i(x, y, z)$  is the normal vector on the body surface;  $S$  is the immersed area of the floating body.

### 3.3. Viscous Damping

The hydrodynamic properties predicted by ANSYS-AQWA are potential results. With the load response of the platform calculated in STAR-CCM+, which is a viscous-flow solver, the viscous damping was then predicted via forced-motion simulation [11].

The flow field has zero initial velocity, which indicates that there is no wave-exciting force acting on the platform. Therefore, radiation and hydrostatic forces are the only fluid forces that act on the platform. The radiation force includes the added inertia force and radiation damping force, which occurs when there are no incoming waves. The total force ( $F_k$ ) that acts on the floating body, which is obtained from the result of the viscous-flow modeling in STAR-CCM+, is expressed in terms of the generalized displacement ( $x_k$ ), as shown below:

$$F_k = A_k x_k'' + B_k x_k' + C_k x_k. \quad (3)$$

From (5),  $x_k$ ,  $x_k'$ , and  $x_k''$  are expressed as follows:

$$x_k = -\zeta \cos(\omega t), \quad (4)$$

$$x_k' = \zeta \omega \sin(\omega t), \quad (5)$$

$$x_k'' = \zeta \omega^2 \cos(\omega t). \quad (6)$$

With the help of Equations (4)–(6), (6) is rewritten as follows:

$$F_k = \zeta \left( (\omega^2 A_k - C_k) \cos(\omega t) + \omega B_k \sin(\omega t) \right) = D_k \cos(\omega t + \varphi_k), \quad (7)$$

where  $D_k$  is the amplitude of  $F_k$ , and  $\varphi_k$  is the phase difference between  $x_k''$  and  $F_k$ , as shown in Figure 7. Therefore,  $A_k$  and  $B_k$  are determined by  $D_k$  and  $\varphi_k$ , as follows:

$$D_k = \sqrt{(\omega^2 A_k - C_k)^2 + (\omega B_k)^2}, \quad (8)$$

$$\varphi_k = \tan^{-1} \frac{-\omega B_k}{\omega^2 A_k - C_k} \quad (9)$$

$$A_k = \frac{C_k + D_k \cos \varphi_k}{\omega^2}, \quad (10)$$

$$B_k = \frac{-D_k \sin \varphi_k}{\omega}, \quad (11)$$

where  $C_k$  comes from the result of AQWA.

Assuming that  $A_{ij}$  is the sum of  $A_{ij,p}$  and  $A_{ij,v}$ ,  $B_{ij}$  is the sum of  $B_{ij,p}$  and  $B_{ij,v}$ , where  $A_{ij,p}$  and  $B_{ij,p}$  are the potential components predicted via the potential-flow theory in AQWA, and  $A_{ij,v}$  and  $B_{ij,v}$  are the viscous components,  $A_k$  and  $B_k$ , (i.e.,  $A_{ij}$  and  $B_{ij}$  are obtained from the results of STAR-CCM+). The detailed viscous-flow formulation and setup are included in Appendix A.

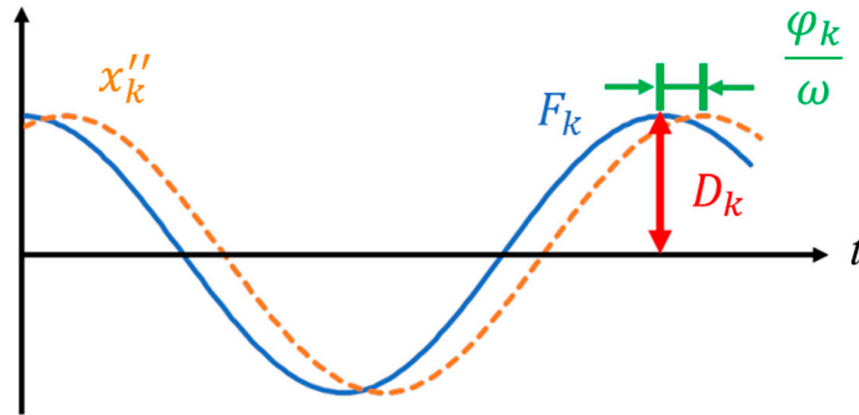


**Figure 7.** Schematic of phase difference between force and acceleration.

### 3.4. Modeling of Floating Wind Turbine System

#### 3.4.1. Aerodynamic Modeling

The aerodynamic loading of a wind turbine is calculated in OrcaFlex using the blade element momentum theory [42], which is a combination of the momentum theory and blade element theory. The thrust force ( $T_r$ ) and moment ( $dQ$ ) on the actuator disk derived by the axial momentum theory are expressed as follows:

$$T_r = \frac{1}{2} \rho A U_{in}^2 4a(1 - a), \tag{12}$$

$$dQ = 4a'(1 - a) \frac{1}{2} \rho U_{in} \omega r^2 2\pi r dr, \tag{13}$$

where  $\rho$  is the fluid density,  $A$  is the disk area,  $U_{in}$  is the inflow velocity, and  $r$  is the radius of the cross section. The axial induction factor ( $a$ ) and angular velocity induction factor ( $a'$ ) are defined as follows:

$$a = \frac{U_{in} - U_1}{U_{in}}. \tag{14}$$

$$a' = \frac{\omega'}{2\omega} \tag{15}$$

where  $U_1$  is the velocity before the fluid flows into the actuator disk. The axial force ( $dF_a$ ) and moment ( $dQ$ ) that act on a blade section derived by the blade element theory are expressed as follows:

$$dF_a = n_b c \frac{1}{2} \rho U^2 [C_l \cos(\theta) + C_d \sin(\theta)] dr, \tag{16}$$

$$dQ = n_b c \frac{1}{2} \rho U^2 [C_l \sin(\theta) - C_d \cos(\theta)] r dr, \tag{17}$$

where  $n_b$  is the number of blades,  $c$  is the chord length of the blade section,  $r$  is the radius of the blade section, and  $C_d$  and  $C_l$  are the drag and lift coefficients, respectively. The relative inflow velocity ( $U$ ) is defined as follows:

$$U = \frac{U_{in}(1 - a)}{\sin(\theta)}, \tag{18}$$

where  $\theta$  is the relative inflow angle. Because  $dT_r$  from the axial momentum theory is equal to  $dF_a$  from the blade element theory, and  $dQ$  from the angular momentum theory is equal

to  $dQ$  from the blade element theory,  $a$  and  $a'$  are expressed as the following equations by combining (15) and (19), and (16) and (20):

$$a = \frac{1}{1 + \frac{4 \sin^2 \theta}{\sigma [C_l \cos(\theta) + C_d \sin(\theta)]}}, \tag{19}$$

$$a' = \frac{1}{\frac{2 \sin(\theta) \cos(\theta)}{\sigma [C_l \cos(\theta) + C_d \sin(\theta)]} - 1}, \tag{20}$$

$$\sigma = \frac{n_b c}{2\pi r}, \tag{21}$$

where  $\sigma$  is the local solidity. The total thrust force and mechanical power are subsequently obtained:

$$T_r = \int_{r_h}^{R_r} dT_r, \tag{22}$$

$$P = \int_{r_h}^{R_r} \omega dQ, \tag{23}$$

where  $r_h$  is the hub radius, and  $R_r$  is the rotor radius.

### 3.4.2. Control System Modeling

The control system modeling for the wind turbine in OrcaFlex is a proportional integral derivative (PID) controller that is supported through Python [42]. It involves the design of two controllers: the generator torque controller and full-span rotor-collective blade pitch controller. The former is designed for the range below the rated wind speed, while the latter is designed for the range above the rated wind speed. Figure 8 shows the schematic of the employed control system.

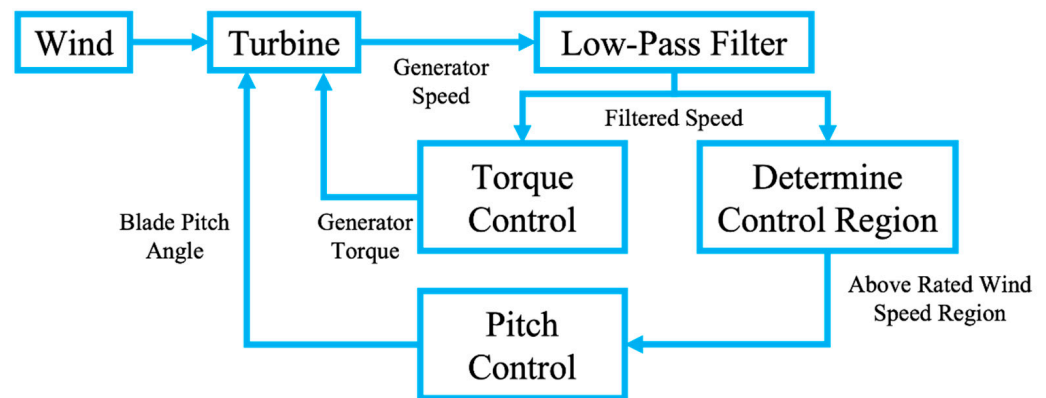


Figure 8. Schematic of employed control system.

### 3.4.3. Mooring Modeling

The finite element method is used for the mooring line modeling in OrcaFlex [42]. The line is divided into a series of straight massless model segments with a node at each end, and each segment models only the axial and torsional properties of the line. It turns out that the axial force predominates in the mooring system. Each line segment is divided into two subsegments, and the properties of each subsegment, such as the mass, weight, and buoyancy, are lumped to the neighboring node.

The axial force contains the effective tension ( $T_e$ ) and wall tension ( $T_w$ ), which are correlated using the following equation:

$$T_e = T_w + (p_{ex}a_{ex} - p_{in}a_{in}), \tag{24}$$

where  $p_{ex}$  and  $p_{in}$  are the external and internal pressure, respectively, and  $a_{ex}$  and  $a_{in}$  are the external and internal cross-sectional stress areas, respectively. The wall tension is obtained as follows:

$$T_w = EA\varepsilon - 2\nu(p_{ex}a_{ex} - p_{in}a_{in}) + k_{tt}\frac{\tau}{l_0} + EA c_d \frac{dl}{dt} \frac{1}{l_0}, \tag{25}$$

$$\varepsilon = \frac{l - \lambda_s l_0}{\lambda_s l_0}, \tag{26}$$

where  $EA$  is the axial stiffness of the line;  $\varepsilon$  is the total mean axial strain;  $\nu$  is the Poisson ratio;  $k_{tt}$  is the coefficient for the torque coupling tension;  $\tau$  is the segment twist angle;  $l$  is the segment length;  $l_0$  is the initial segment length;  $\lambda_s$  is the expansion factor of the segment;  $c_d$  is the damping coefficient for the mooring line, which is defined as follows:

$$c_d = \frac{\lambda_a}{100} c_c, \tag{27}$$

$$c_c = \sqrt{\frac{2ml_0}{EA}}, \tag{28}$$

where  $\lambda_a$  is the target tension damping,  $c_c$  is the critical damping value for a segment, and  $m$  is the segment mass including the contents but not of any attachment.

#### 4. Performance Prediction

##### 4.1. Case Description

The performance of a 15 MW floating wind turbine system using the semisubmersible Taida floating platform equipped with an IEA 15 MW offshore wind turbine predicted via the potential-flow approach (PF approach), which only considers the potential result, and the viscous-flow approach (VF approach), which additionally considers the effects of the viscosity, in the Hsinchu offshore area is presented in this study. The irregular wave conditions discussed in this study correspond to the wave scatter diagram of the Hsinchu offshore area, which is shown in Table 4 [35], in which the significant wave height is  $H_s$  and the zero-crossing period is  $T_z$ . In this study, the common wave condition (CW condition) (i.e.,  $(H_s, T_z) = (1.5 \text{ m}, 5.5 \text{ s})$ ) and high wave condition (HW condition) (i.e.,  $(H_s, T_z) = (4.5 \text{ m}, 7.5 \text{ s})$ ) were both considered. According to [39], the JONSWAP spectrum with  $\gamma = 2.08$  was chosen as the wave spectrum. The wind profile (Figure 9) and current profile of an offshore area are defined as follows:

$$U_{in}^w = U_w \left( \frac{z}{H_h} \right)^{0.1}, \tag{29}$$

$$U_{in}^c = U_c \left( \frac{z+h}{h} \right)^{\frac{1}{7}}, \tag{30}$$

where  $U_w$  is the wind velocity at the hub height;  $U_{in}^w$  is the wind velocity;  $U_c$  is the current velocity at the free surface;  $U_{in}^c$  is the current velocity;  $z$  is the height above mean sea level;  $H_h$  is the hub height of an IEA 15 MW wind turbine ( $H_h = 150 \text{ m}$ );  $h$  is the water depth ( $h = 70 \text{ m}$ ). The wind velocity obtained from the Beaufort scale ( $U_B$ ) is the wind velocity defined at 10 m above MSL, and the  $U_w$  is then calculated via (32). According to [16], the surface current speed ( $U_c$ ) was assumed to be 0.93 m/s, which occurs in the Taiwan Strait with a probability of 75%. The metocean conditions adopted in this study are summarized in Table 5. The waves were assumed to have a direction consistent with the wind. In this study, seven wind and wave directions ( $\theta_w = 0^\circ, 30^\circ, \dots, 180^\circ$ ) and four current directions ( $\theta_c = 0^\circ, 90^\circ, 180^\circ, 270^\circ$ ) are discussed. The wind, wave, and current directions are defined as the angles measured counterclockwise from the positive  $x$ -axis to the incoming wind or current directions, as shown in Figure 10.

**Table 4.** Wave scatter diagram of Hsinchu offshore area.

$H_s$ (m)	$T_z$ (s)					Sum
	3.5	4.5	5.5	6.5	7.5	
0.5	14.79%	41.96%	5.49%	0.44%	0.02%	62.7%
1.5	0.31%	12.23%	18.31%	0.70%	-	31.55%
2.5	-	0.02%	4.35%	0.90%	0.04%	31.55%
3.5	-	-	-	0.35%	0.04%	5.32%
4.5	-	-	-	0.04%	0.02%	0.07%
Sum	15.10%	54.21%	28.15%	2.43%	0.11%	100%

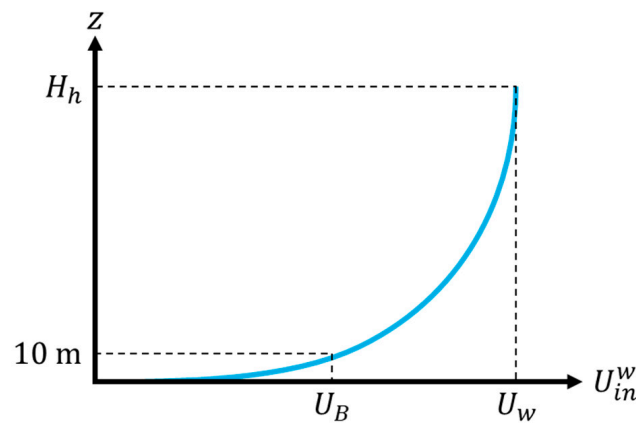


**Figure 9.** Schematic illustration of wind profile.

**Table 5.** Metocean conditions of two irregular wave conditions.

Properties (Unit)	CW Condition	HW Condition
$\gamma$ for JONSWAP Spectrum	2.08	2.08
$H_s$ (m)	1.5	4.5
$T_z$ (s)	5.5	7.5
$U_B$ (m/s)	8.11	17.8
$U_w$ (m/s)	10.63	23.34
$U_c$ (m/s)	0.93	0.93

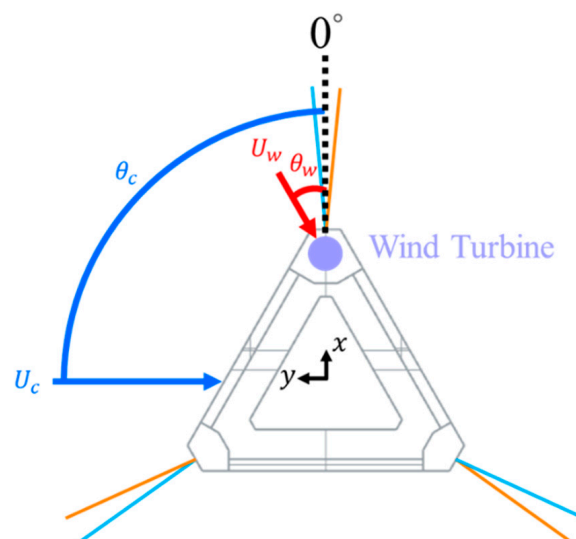


**Figure 10.** Definition of wind, wave, and current directions.

### 4.2. Hydrodynamic Properties

This study estimated the hydrodynamic properties of the Taida platform in the frequency domain from 0 Hz to 0.5 Hz via AQWA. STAR-CCM+ was then employed to obtain the load response of the platform under forced motion in the viscous-flow field to predict the viscous damping. The comparison between the hydrodynamic properties via the PF approach and VF approach (i.e.,  $A_{ij,p}$  vs.  $A_{ij}$ , and  $B_{ij,p}$  vs.  $B_{ij}$ ) is shown in Figures 11 and 12. The mean value of the hydrodynamic properties of the last five periods of a forced motion was employed in the viscous damping prediction, and only the nonnegative predicted result was used.

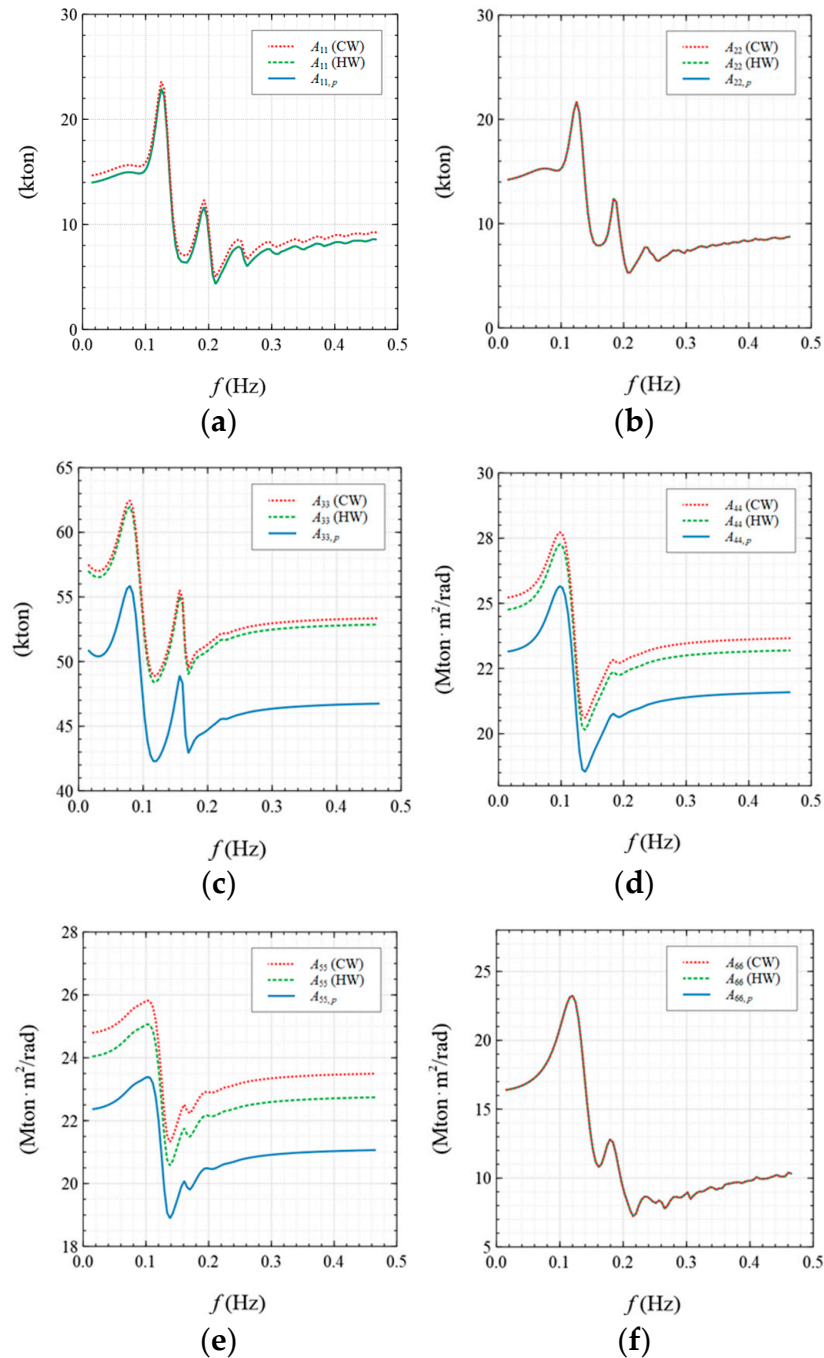


**Figure 11.** Comparison of added masses in different motion directions: (a) surge; (b) sway; (c) heave; (d) roll; (e) pitch; (f) yaw.

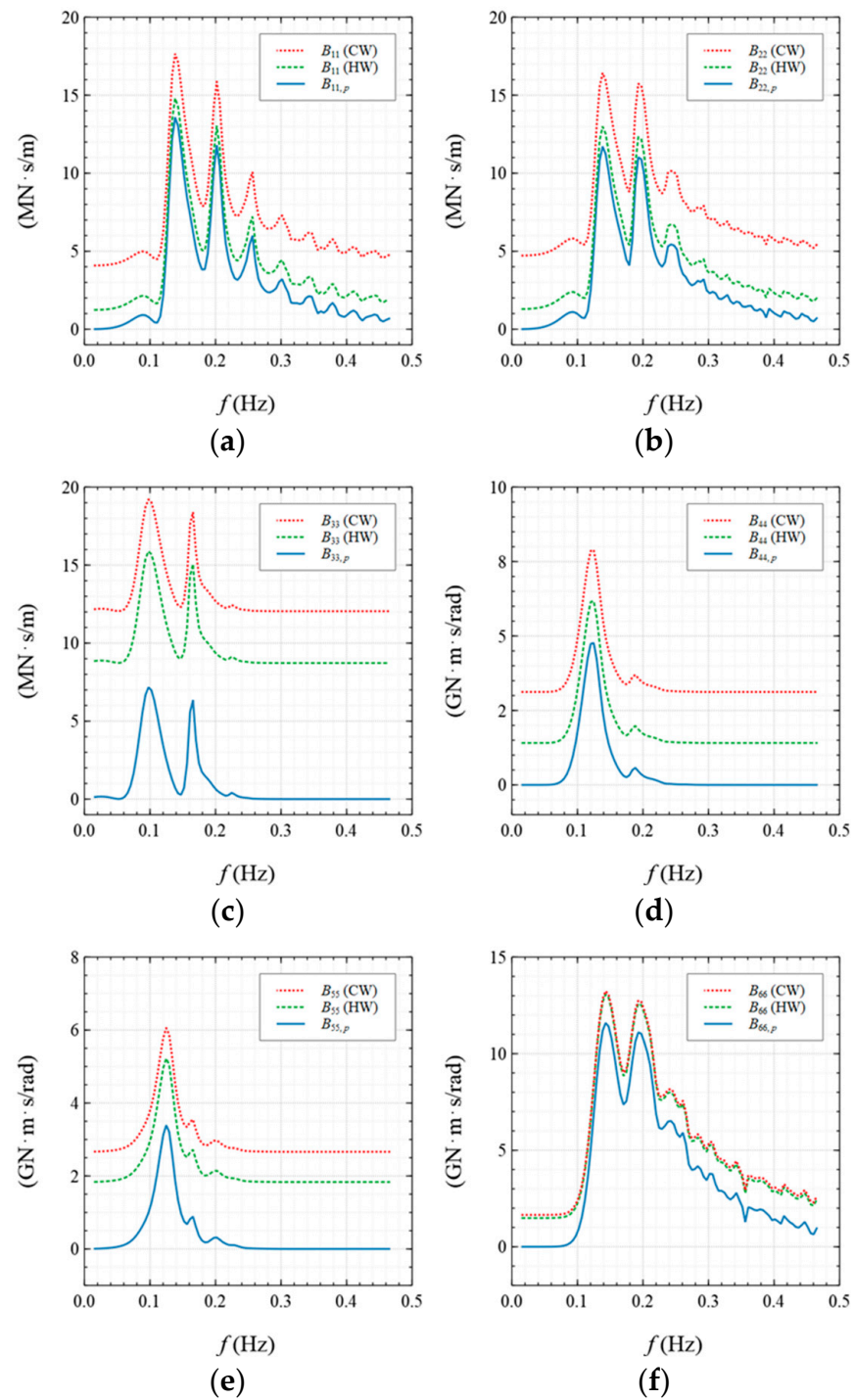


**Figure 12.** Comparison of damping in different motion directions: (a) surge; (b) sway; (c) heave; (d) roll; (e) pitch; (f) yaw.

Under the CW condition ( $T_z = 5.5$  s), the heave motion has an added mass of around 51 kton, which is the largest among the translation motions, while the surge and sway motions have added masses of around 12 kton and 10 kton, respectively. Among the rotation motions, the roll and pitch motions have added masses of around 23 Mton·m<sup>2</sup>/rad, while the yaw motion has an added mass of around 13 Mton·m<sup>2</sup>/rad. The heave motion has a damping of around 14 MN·s/m, which is the largest among the translation motions, while the surge and sway motions have damping values of around 10 MN·s/m and 8 MN·s/m, respectively. The yaw motion has a damping of around 11 GN·m·s/rad, which is the largest among the rotation motions, while the roll and pitch motions have damping values

of around 3 GN·m·s/rad and 4 GN·m·s/rad, respectively. The added mass of the heave motion predicted via the viscous-flow approach is up to 15% higher than that predicted via the potential-flow approach. The damping of the roll motion predicted via the viscous-flow approach is up to about 14 times that predicted via the potential-flow approach.

Under the HW condition ( $T_z = 7.5$  s), the heave motion has an added mass of around 50 kton, which is the largest among the translation motions, while the surge and sway motions have added masses of around 18 kton and 19 kton, respectively. The roll motion has an added mass of around 21 Mton·m<sup>2</sup>/rad, which is the largest among the rotation motions, while the pitch and yaw motions have added masses of around 20 Mton·m<sup>2</sup>/rad. The sway motion has a damping of around 13 MN·s/m, which is the largest among the translation motions, while the surge and heave motions have damping values of around 11 MN·s/m and 10 MN·s/m, respectively. The yaw motion has a damping of around 11 GN·m·s/rad, which is the largest among the rotation motions, while the roll and pitch motions have damping values of around 5 GN·m·s/rad. The added mass of the heave motion predicted via the viscous-flow approach is up to 14% higher than that predicted via the potential-flow approach. The damping of the heave motion predicted via the viscous-flow approach is up to about 7 times that predicted via the potential-flow approach.

The prediction result shows that the viscous effect has a larger impact on the hydrodynamic properties in the heave, roll, and pitch motions than in the surge, sway, and yaw motions. The viscous effects that impact the hydrodynamic properties under the CW condition are larger than those under the HW condition.

#### 4.3. Motion Response and Generator Power

The motion response and generator power were obtained by solving the equations of the motions in OrcaFlex.  $\eta_i$  represents the linear and angular displacement in the 6 dof motions, where  $i = 1, 2, \dots, 6$  refer to the surge, sway, heave, roll, pitch, and yaw motions, respectively. Moreover, because the simulations were conducted under irregular wave conditions in the time domain, the raw data are presented in time series for 1000 s. Figure 13 presents the pitch motion and power output under  $\theta_w = 0^\circ$  and  $\theta_c = 0^\circ$ , where the red line denotes the CW response, and the blue line represents the HW result. The randomness in the responses as well as the greater fluctuation can be seen in the HW results with different means. The following sections use the means (a bar on the variable) and standard deviations ( $\sigma$ ) of the motion response, power output, and mooring line tension to characterize the time-domain results.

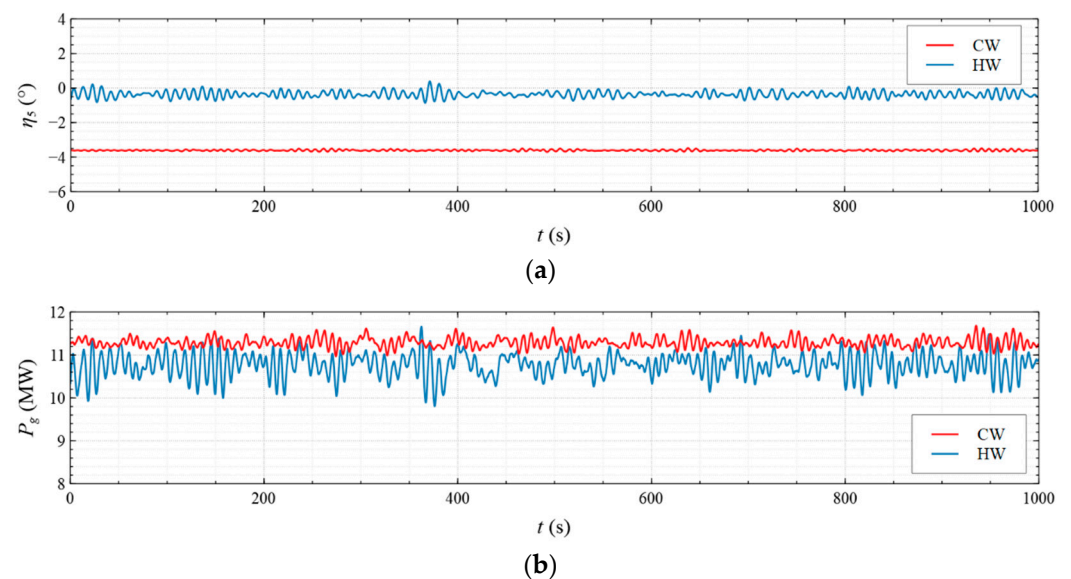


**Figure 13.** Time histories of (a) pitch motion and (b) power output under  $\theta_w = 0^\circ$  and  $\theta_c = 0^\circ$ .

### 4.3.1. Common Wave Condition

The mean and standard deviation of the platform motions and generator power under the CW condition are shown in Figures 14–20. The largest means of the surge, sway, heave, roll, pitch, and yaw motions of the platform appearing at  $\theta_w = 0^\circ, 90^\circ, 0^\circ, 90^\circ, 180^\circ,$  and  $60^\circ,$  respectively, are  $-6.685\text{ m}, -5.684\text{ m}, -2.168\text{ m}, 6.995^\circ, 4.521^\circ,$  and  $-1.707^\circ,$  respectively. The smallest means of the surge, sway, heave, roll, pitch, and yaw motions of the platform appearing at  $\theta_w = 120^\circ, 0^\circ, 180^\circ, 0^\circ, 90^\circ,$  and  $0^\circ,$  respectively, are  $-0.079\text{ m}, 0.045\text{ m}, -1.392\text{ m}, -0.284^\circ, -0.062^\circ,$  and  $0.076^\circ,$  respectively. The largest standard deviations of the surge, sway, heave, roll, pitch, and yaw motions of the platform appearing at  $\theta_w = 150^\circ, 60^\circ, 0^\circ, 90^\circ, 180^\circ,$  and  $90^\circ,$  respectively, are  $0.153\text{ m}, 0.141\text{ m}, 0.038\text{ m}, 0.089^\circ, 0.057^\circ,$  and  $0.148^\circ,$  respectively. The smallest standard deviations of the surge, sway, heave, roll, pitch, and yaw motions of the platform appearing at  $\theta_w = 90^\circ, 0^\circ, 60^\circ, 180^\circ, 120^\circ,$  and  $0^\circ,$  respectively, are  $0.048\text{ m}, 0.003\text{ m}, 0.025\text{ m}, 0.009^\circ, 0.021^\circ,$  and  $0.003^\circ,$  respectively. The largest mean of the generator power appearing at  $\theta_w = 150^\circ$  is  $14.544\text{ MW},$  followed by the generator power at  $\theta_w = 180^\circ$  and  $120^\circ,$  where the means of the power are up to  $14.461\text{ MW}$  and  $14.409\text{ MW},$  while the smallest mean appearing at  $\theta_w = 0^\circ$  is  $11.282\text{ MW}.$  The largest standard deviation of the generator power appearing at  $\theta_w = 180^\circ$  is  $0.185\text{ MW},$  while the smallest one appearing at  $\theta_w = 0^\circ$  is  $0.104\text{ MW}.$

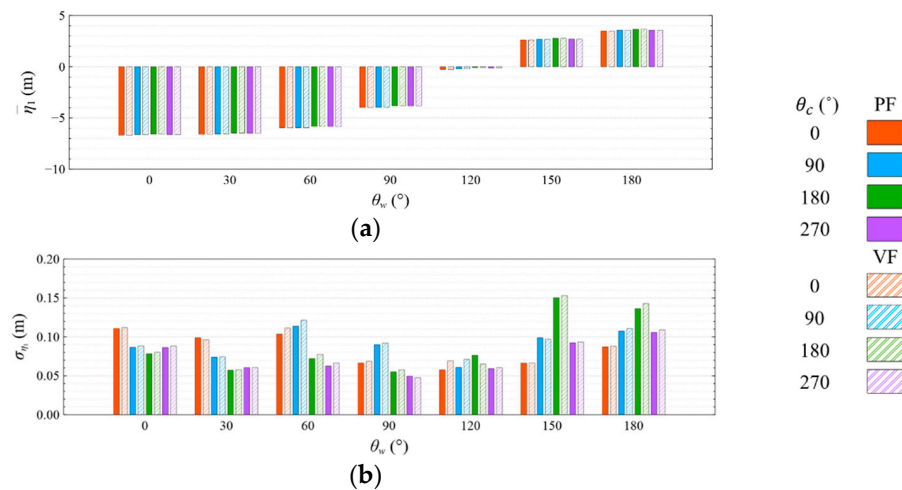


**Figure 14.** Comparison of (a) means and (b) standard deviations of platform surge motion under CW condition.

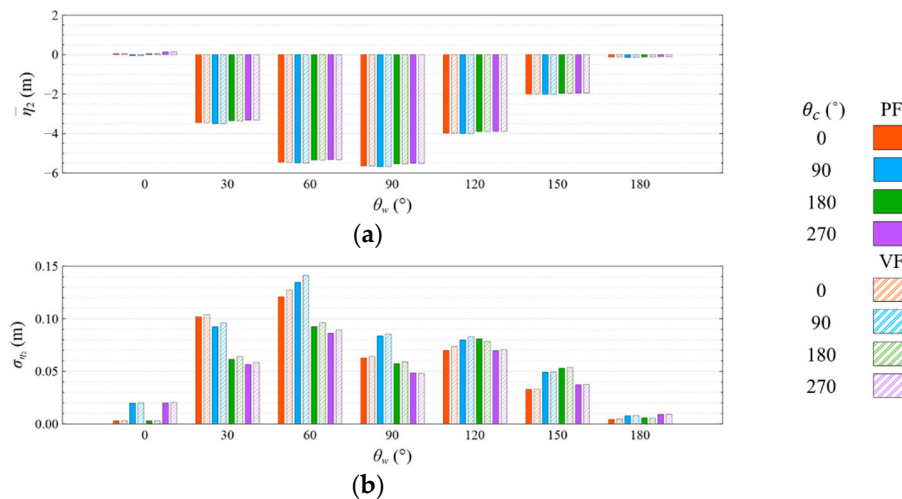


**Figure 15.** Comparison of (a) means and (b) standard deviations of platform sway motion under CW condition.

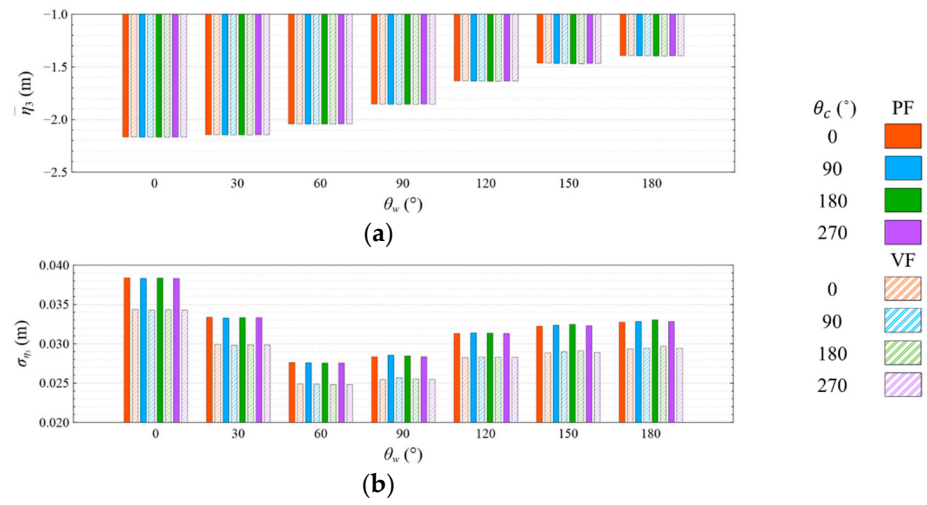


Figure 16. Comparison of (a) means and (b) standard deviations of platform heave motion under CW condition.

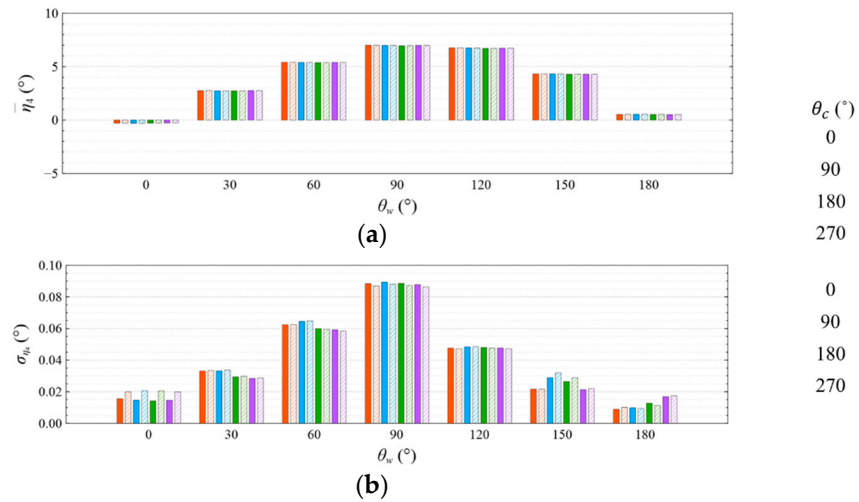


Figure 17. Comparison of (a) means and (b) standard deviations of platform roll motion under CW condition.

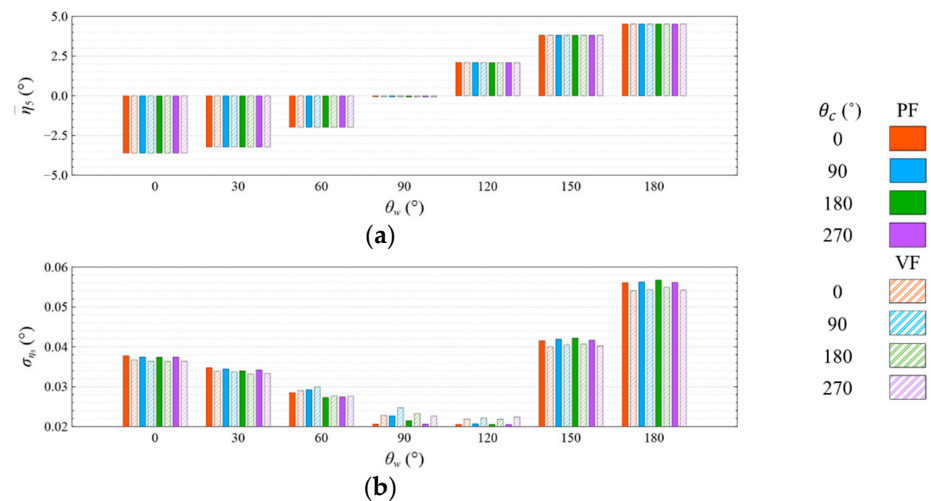
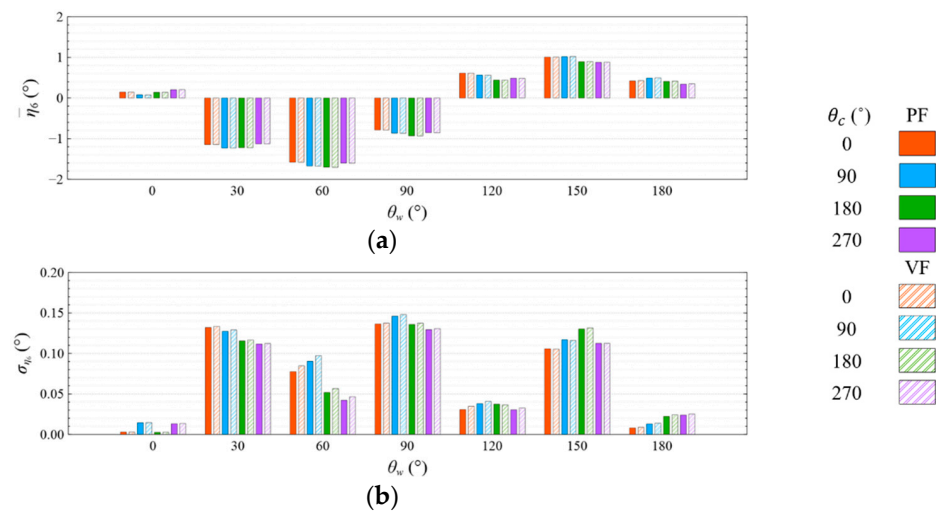
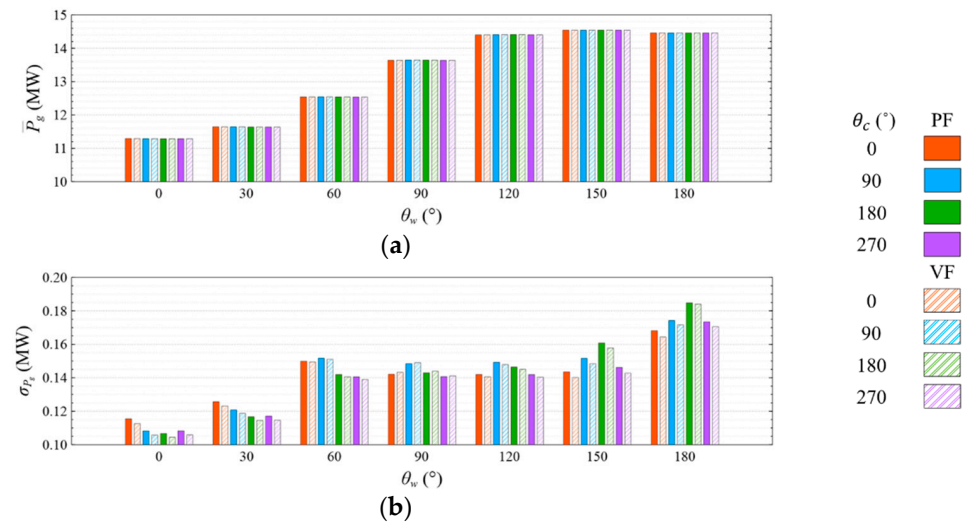


Figure 18. Comparison of (a) means and (b) standard deviations of platform pitch motion under CW condition.



**Figure 19.** Comparison of (a) means and (b) standard deviations of platform yaw motion under CW condition.



**Figure 20.** Comparison of (a) means and (b) standard deviations of generator electrical power under CW condition.

The results shows that the means and standard deviations are sensitive to the wind directions. The performance difference between the two approaches, as well as among the four current directions, are small in terms of the mean value, but relatively substantial in terms of the standard deviation. In conclusion, the generator power is relatively high and stable at  $\theta_w = 120^\circ$  to  $180^\circ$ , and the corresponding motion responses all meet the design requirements discussed in Sections 2.1 and 2.2. Hence,  $\theta_w = 120^\circ$  to  $180^\circ$  is the most favorable wind direction for the studied wind turbine system to operate under the CW condition in the Hsinchu offshore area, where the mean output power can reach 90% of the rated power. The occurrence of the most favorable power performance at  $\theta_w = 120^\circ$  to  $180^\circ$  is clearly explained by the coupled platform motion with the motion-induced and wave-excited components because the center of gravity of the wind turbine system is off its geometrical center.

#### 4.3.2. High Wave Condition

The means and standard deviations of the platform motions and generator power under the HW condition are shown in Figures 21–27. The largest means of the surge, sway, heave, roll, pitch, and yaw motions of the platform appearing at  $\theta_w = 0^\circ, 90^\circ, 30^\circ, 150^\circ,$

180°, and 0°, respectively, are −5.172 m, 3.04 m, −1.855 m, 1.278°, 0.597°, and −3.761°, respectively. The smallest means of the surge, sway, heave, roll, pitch, and yaw motions of the platform appearing at  $\theta_w = 150^\circ, 180^\circ, 180^\circ, 60^\circ, 120^\circ,$  and  $120^\circ,$  respectively, are 0.009 m, −0.227 m, −1.622 m, 0.088°, 0.027°, and 0.053°, respectively. The largest standard deviations of the surge, sway, heave, roll, pitch, and yaw motions of the platform appearing at  $\theta_w = 180^\circ, 60^\circ, 0^\circ, 90^\circ, 180^\circ,$  and  $60^\circ,$  respectively, are 1.241 m, 0.717 m, 0.322 m, 0.406°, 0.242°, and 1.014°, respectively. The smallest standard deviations of the surge, sway, heave, roll, pitch, and yaw motions of the platform appearing at  $\theta_w = 120^\circ, 180^\circ, 90^\circ, 0^\circ, 120^\circ,$  and  $0^\circ,$  respectively, are 0.177 m, 0.039 m, 0.229 m, 0.034°, 0.110°, and 0.096°, respectively. The mean of the generator power is 15 MW (i.e., the rated power at  $\theta_w = 90^\circ, 120^\circ, 150^\circ,$  and  $180^\circ$ ), while the smallest mean appearing at  $\theta_w = 0^\circ$  is 10.751 MW. The largest standard deviation of the generator power appearing at  $\theta_w = 60^\circ$  is 0.385 MW, while the smallest one appearing at  $\theta_w = 120^\circ$  is 0.182 MW.

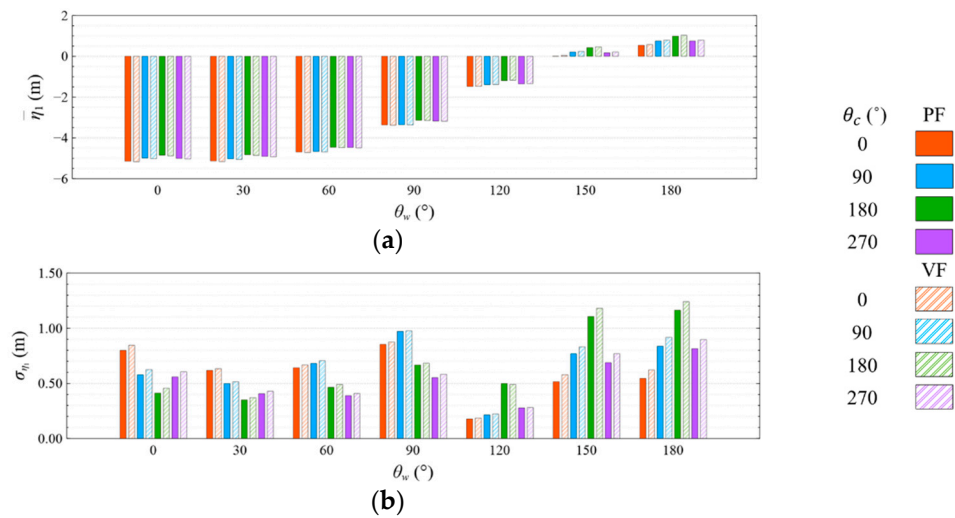


Figure 21. Comparison of (a) means and (b) standard deviations of platform surge motion under HW condition.

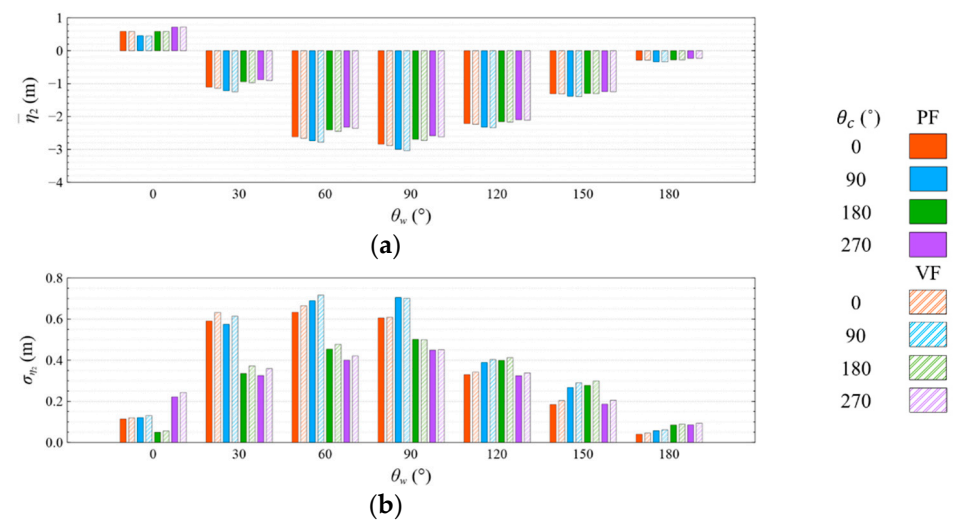


Figure 22. Comparison of (a) means and (b) standard deviations of platform sway motion under HW condition.

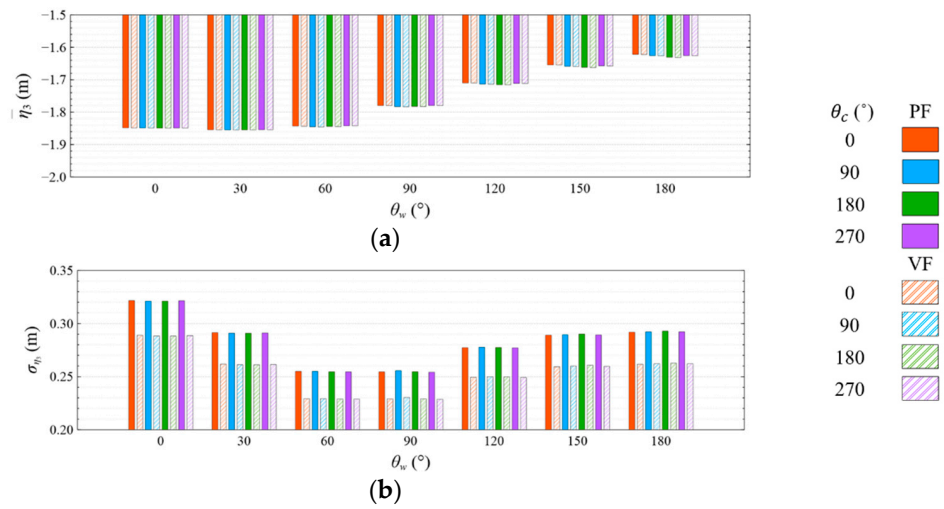


Figure 23. Comparison of (a) means and (b) standard deviations of platform heave motion under HW condition.

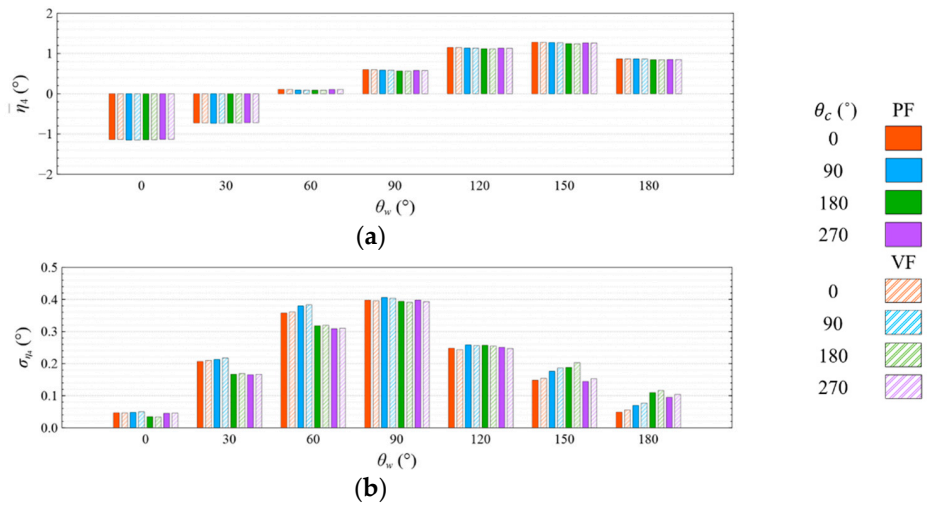


Figure 24. Comparison of (a) means and (b) standard deviations of platform roll motion under HW condition.

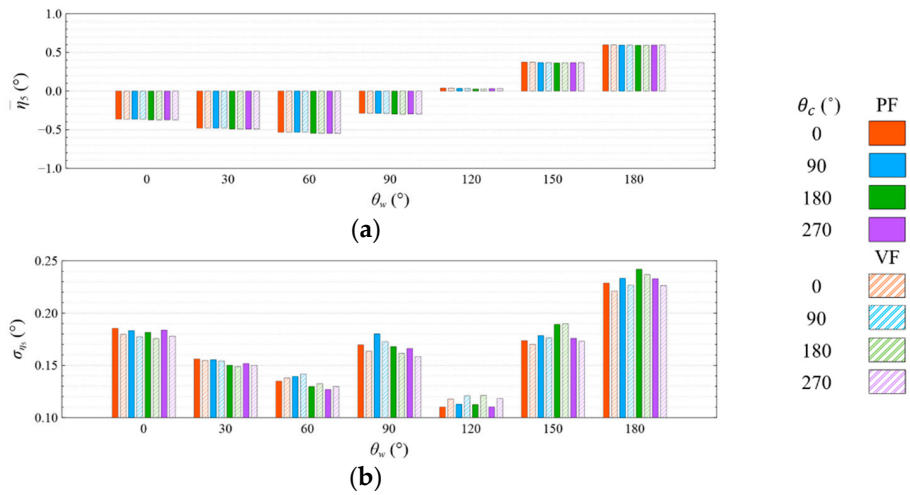
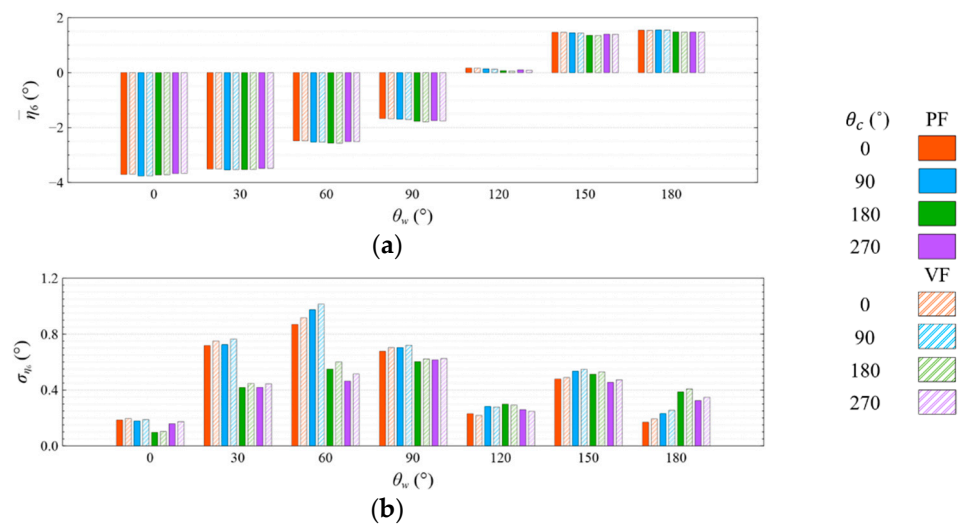
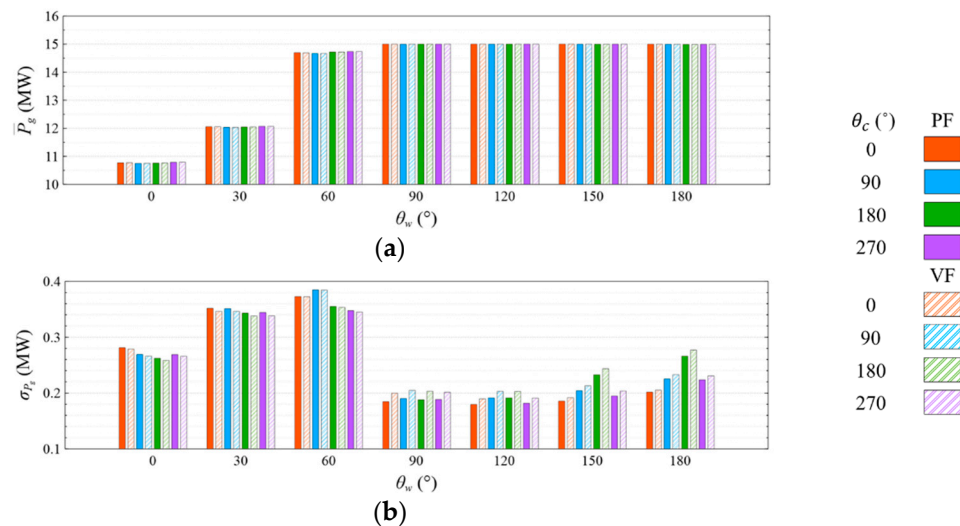


Figure 25. Comparison of (a) means and (b) standard deviations of platform pitch motion under HW condition.



**Figure 26.** Comparison of (a) means and (b) standard deviations of platform yaw motion under HW condition.



**Figure 27.** Comparison of (a) means and (b) standard deviations of generator electrical power under HW condition.

Similar to the CW condition, the mean and standard deviation of the motion response are sensitive to the wind directions, and the performance difference between the two approaches, as well as among the four current directions, are mainly reflected in the standard deviation rather than in the mean value. In conclusion, the generator power is relatively high and stable at  $\theta_w = 60^\circ$  to  $180^\circ$ , and the corresponding motion responses all meet the design requirements discussed in Sections 2.1 and 2.2. Hence,  $\theta_w = 60^\circ$  to  $180^\circ$  is the most favorable wind direction for the studied wind turbine system to operate under the HW condition in the Hsinchu offshore area, where the mean output power can reach 95% of the rated power. When compared with the CW results, it is obvious that the increase in the wind speed extends the favorable operation range in the incoming wind direction, as well as enhances the mean output power.

#### 4.4. Mooring Line Tension

##### 4.4.1. Common Wave Condition

The means and standard deviations of the mooring line tension under the CW condition are shown in Figures 28–33. The largest means of the mooring line tension of Lines A1, A2, B1, B2, C1, and C2 appearing at  $\theta_w = 30^\circ, 0^\circ, 150^\circ, 120^\circ, 180^\circ,$  and  $180^\circ$ , respectively,

are 1.768 MN, 1.703 MN, 2.001 MN, 1.833 MN, 1.369 MN, and 1.817 MN, respectively. The smallest means of the mooring line tension of Lines A1, A2, B1, B2, C1, and C2 appearing at  $\theta_w = 180^\circ, 180^\circ, 0^\circ, 0^\circ, 60^\circ,$  and  $60^\circ$ , respectively, are 0.445 MN, 0.448 MN, 0.588 MN, 0.576 MN, 0.317 MN, and 0.321 MN, respectively. The largest standard deviations of the mooring line tension of Lines A1, A2, B1, B2, C1, and C2 appearing at  $\theta_w = 60^\circ, 0^\circ, 150^\circ, 120^\circ, 150^\circ,$  and  $150^\circ$ , respectively, are 0.038 MN, 0.031 MN, 0.037 MN, 0.031 MN, 0.023 MN, and 0.043 MN, respectively. The smallest standard deviations of the mooring line tension of Lines A1, A2, B1, B2, C1, and C2 appearing at  $\theta_w = 180^\circ, 180^\circ, 0^\circ, 0^\circ, 0^\circ,$  and  $0^\circ$ , respectively, are all around 3 kN.

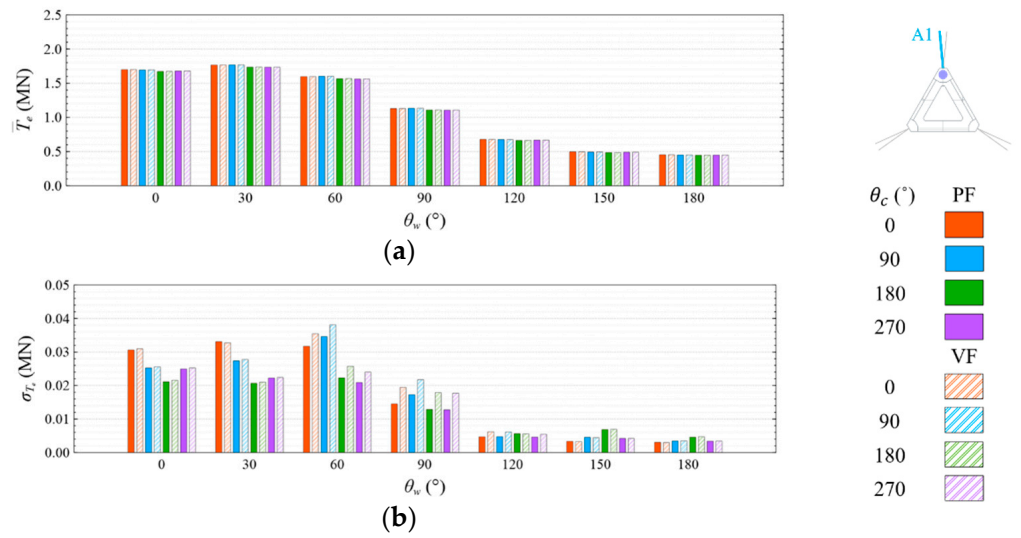


Figure 28. Comparison of (a) means and (b) standard deviations of mooring line tension of Line A1 under CW condition.

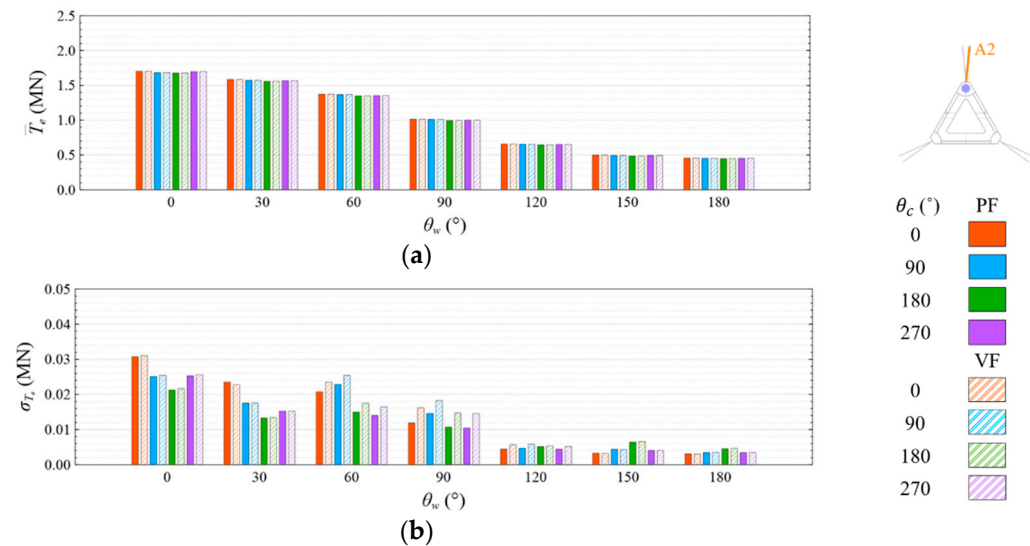


Figure 29. Comparison of (a) means and (b) standard deviations of mooring line tension of Line A2 under CW condition.

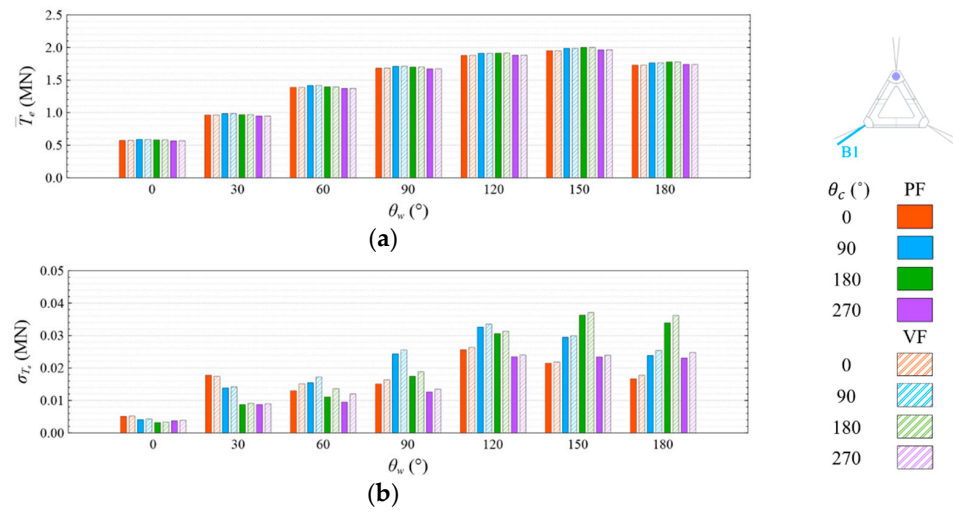


Figure 30. Comparison of (a) means and (b) standard deviations of mooring line tension of Line B1 under CW condition.

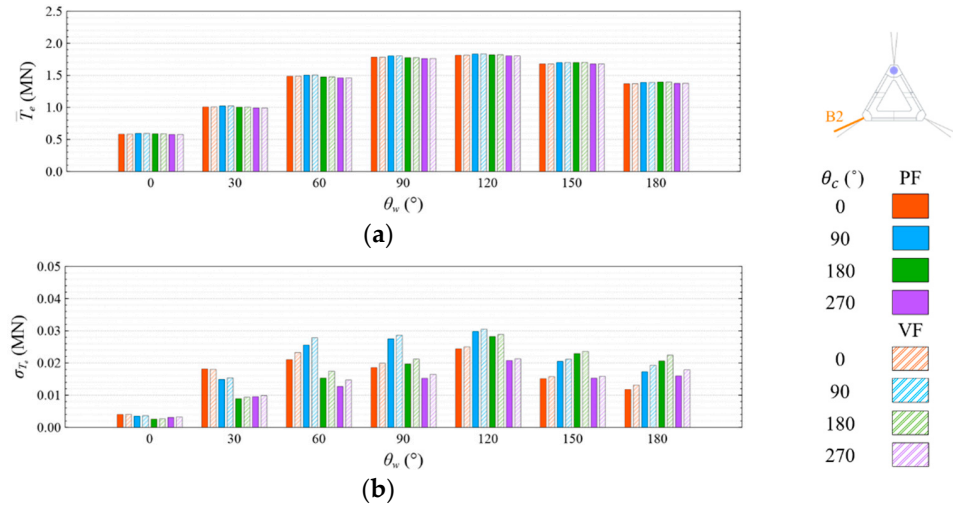


Figure 31. Comparison of (a) means and (b) standard deviations of mooring line tension of Line B2 under CW condition.

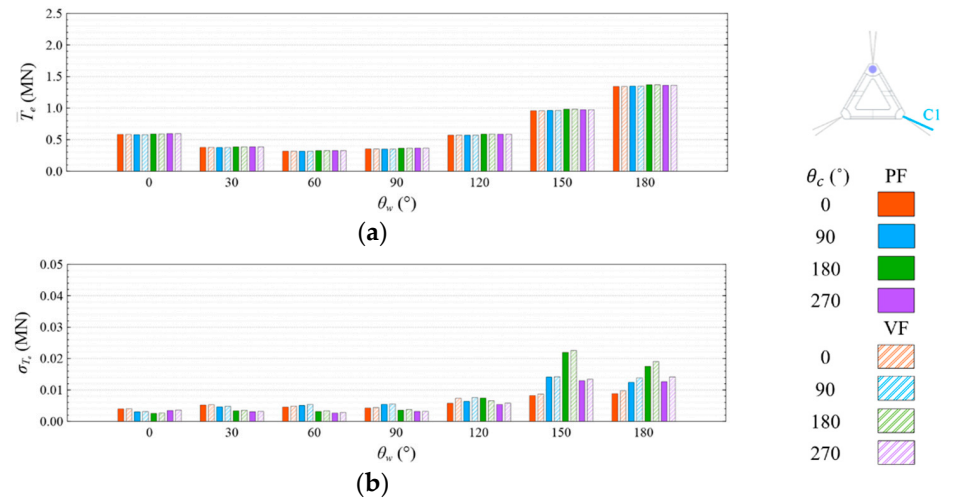
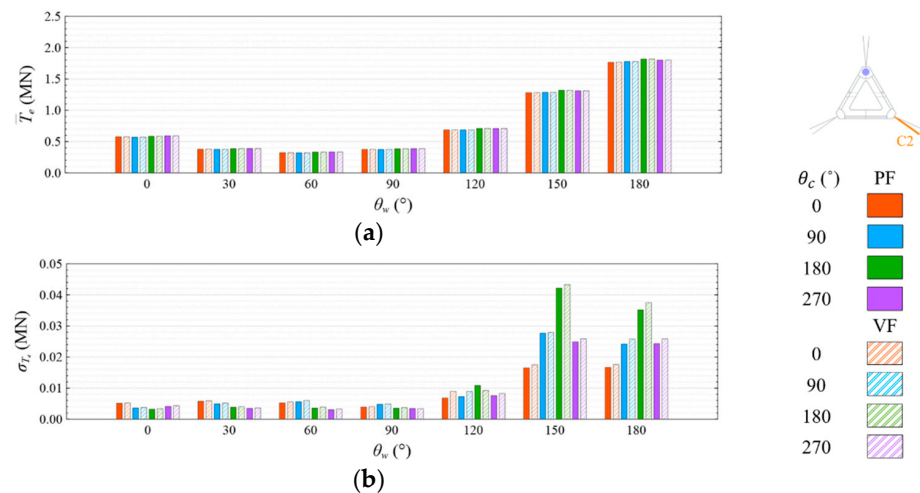


Figure 32. Comparison of (a) means and (b) standard deviations of mooring line tension of Line C1 under CW condition.



**Figure 33.** Comparison of (a) means and (b) standard deviations of mooring line tension of Line C2 under CW condition.

Similar to the motion response and generator power, the mooring line tension difference in the mean value between the two approaches, as well as among the four current directions, is clearly smaller than that in the standard deviation. The sums of the means and standard deviations of the mooring line tensions under the CW condition are all smaller than one-seventh of the break load of the mooring line.

#### 4.4.2. High Wave Condition

The means and standard deviations of the mooring line tension under the CW condition are shown in Figures 34–39. The largest means of the mooring line tension of Lines A1, A2, B1, B2, C1, and C2 appearing at  $\theta_w = 30^\circ, 0^\circ, 150^\circ, 120^\circ, 180^\circ$ , and  $180^\circ$ , respectively, are 1.426 MN, 1.273 MN, 1.473 MN, 1.314 MN, 1.077 MN, and 1.4 MN, respectively. The smallest means of the mooring line tension of Lines A1, A2, B1, B2, C1, and C2 appearing at  $\theta_w = 180^\circ, 180^\circ, 0^\circ, 0^\circ, 60^\circ$ , and  $60^\circ$ , respectively, are 0.594 MN, 0.607 MN, 0.683 MN, 0.608 MN, 0.474 MN, and 0.458 MN, respectively. The largest standard deviations of the mooring line tension of Lines A1, A2, B1, B2, C1, and C2 appearing at  $\theta_w = 0^\circ, 0^\circ, 180^\circ, 180^\circ, 150^\circ$ , and  $180^\circ$ , respectively, are 0.174 MN, 0.157 MN, 0.088 MN, 0.155 MN, 0.129 MN, and 0.246 MN, respectively. The smallest standard deviations of the mooring line tension of Lines A1, A2, B1, B2, C1, and C2 appearing at  $\theta_w = 120^\circ, 120^\circ, 0^\circ, 0^\circ, 0^\circ$ , and  $120^\circ$ , respectively, are 0.015 MN, 0.019 MN, 0.063 MN, 0.02 MN, 0.024 MN, and 0.026 MN, respectively.

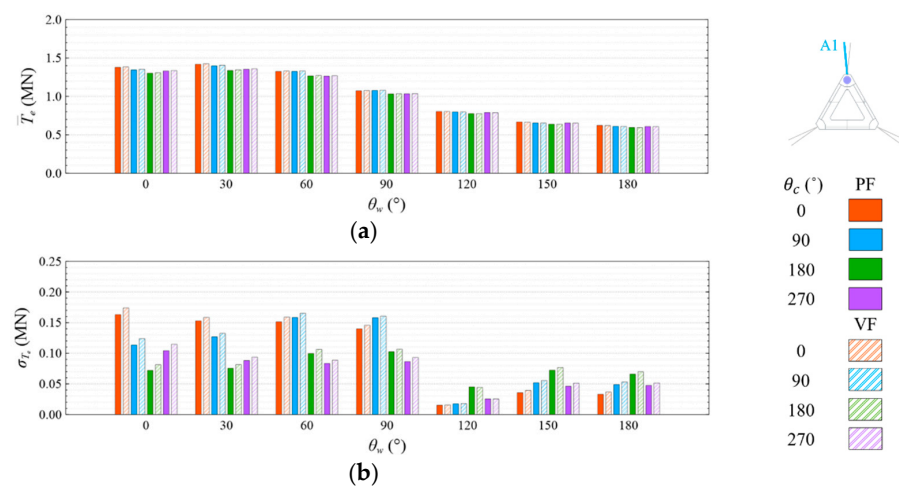


**Figure 34.** Comparison of (a) means and (b) standard deviations of mooring line tension of Line A1 under HW condition.

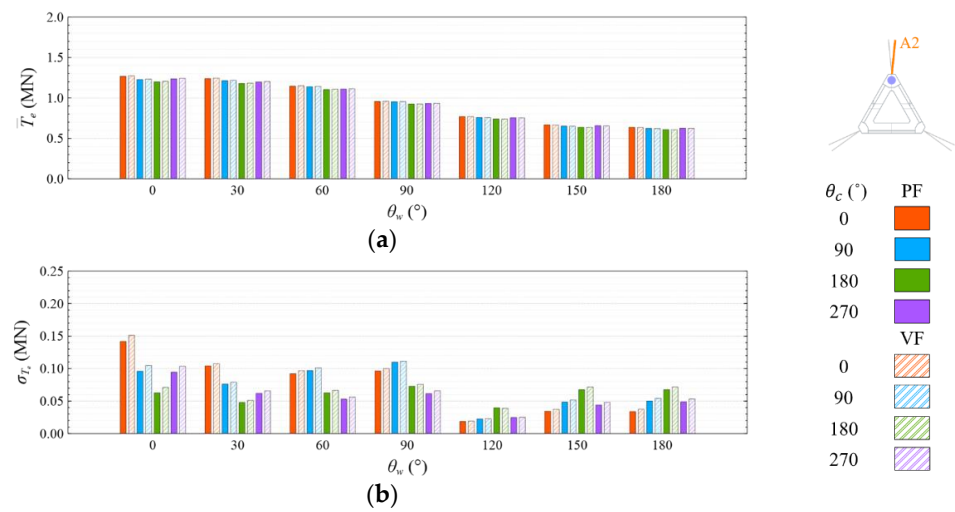


Figure 35. Comparison of (a) means and (b) standard deviations of mooring line tension of Line A2 under HW condition.

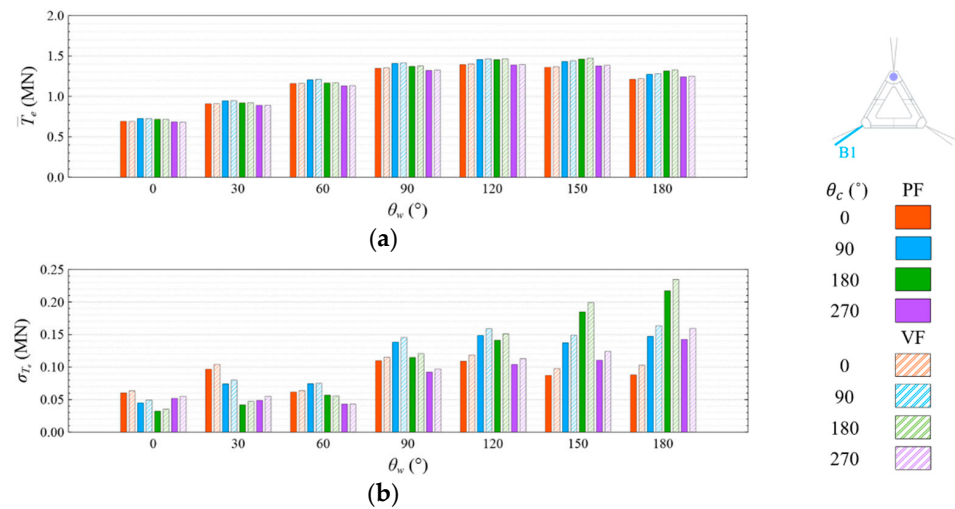


Figure 36. Comparison of (a) means and (b) standard deviations of mooring line tension of Line B1 under HW condition.

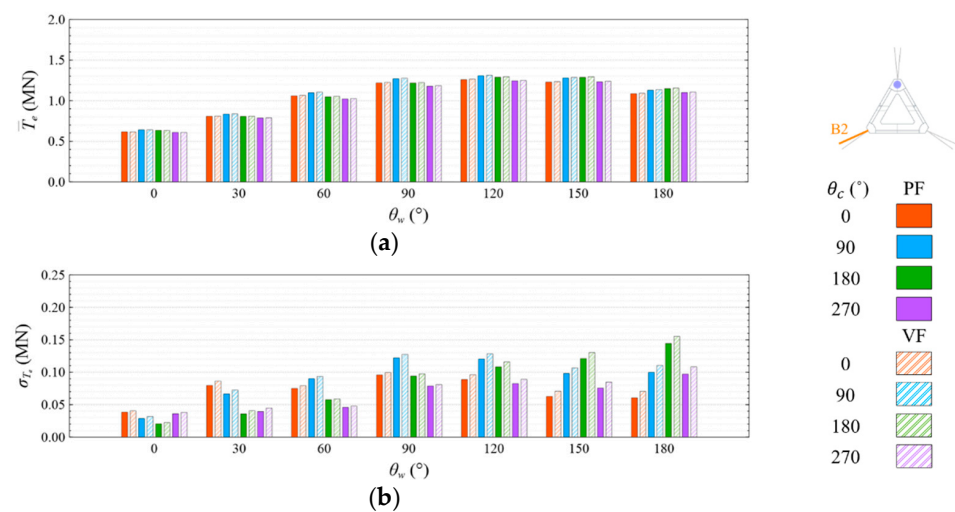
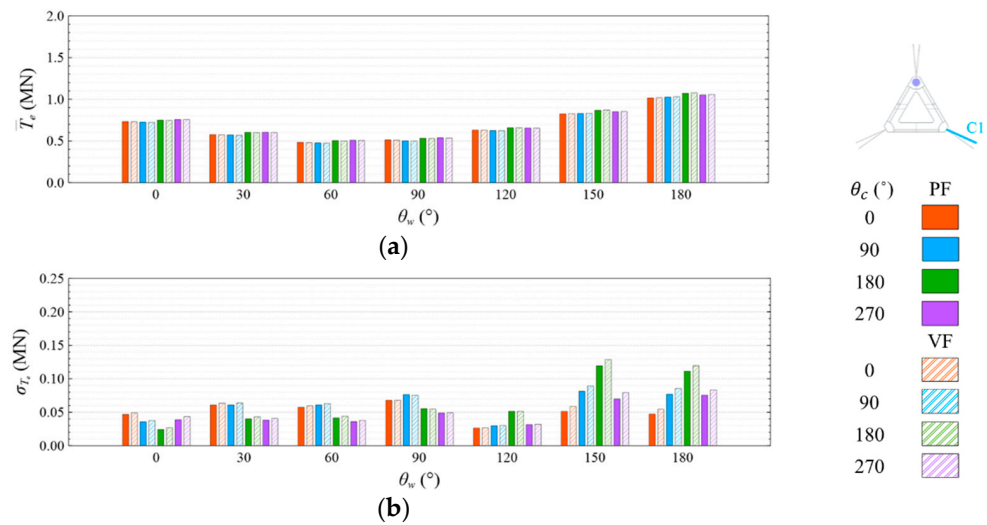
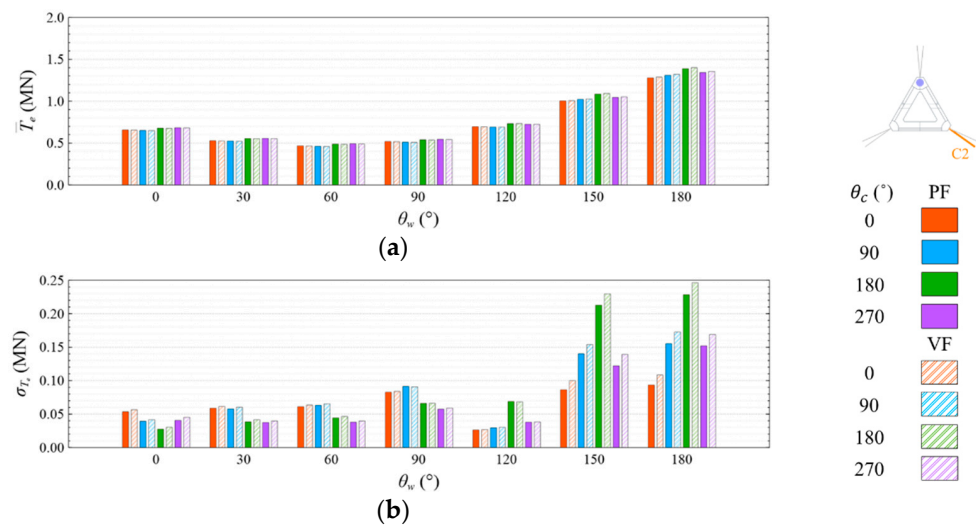


Figure 37. Comparison of (a) means and (b) standard deviations of mooring line tension of Line B2 under HW condition.



**Figure 38.** Comparison of (a) means and (b) standard deviations of mooring line tension of Line C1 under HW condition.



**Figure 39.** Comparison of (a) means and (b) standard deviations of mooring line tension of Line C2 under HW condition.

Similar to the motion response and generator power, the mooring line tension difference in the mean value between the two approaches, as well as among the four current directions, is smaller than that in the standard deviation. The sums of the means and standard deviations of the mooring line tensions under the HW condition are all smaller than one-eighth of the break load of the mooring line.

### 5. Conclusions

This study aimed to predict the motion response and power performance of a 15 MW floating wind turbine system equipped with a semisubmersible Taida floating platform, an IEA 15 MW offshore wind turbine, and a  $3 \times 2$  mooring design under the metocean conditions of the Hsinchu offshore area in the Taiwan Strait. We first compared the potential and viscous results of the hydrodynamic properties. We then compared the means and standard deviations of the motion response, generator power, and mooring line tension via the potential- and viscous-flow approaches, for which the combinations of seven wind directions and four current directions under two wave conditions were considered. The results of this study are summarized below:

1. The viscous effect has a more substantial impact on the hydrodynamic properties in the heave, roll, and pitch motions than in the surge, sway, and yaw motions. The viscous impact on the hydrodynamic properties under the CW condition is larger than that under the HW condition. The viscous prediction of the added mass in the heave motion increases by up to 15% of the potential result under the CW condition, while that in the heave motion under the HW condition increases by up to 14%. The viscous damping prediction in the roll motion increases by up to 13 times the potential result under the CW condition, while that in the heave motion under the HW condition increases by up to 6 times;
2. The viscous effect has a more substantial impact on the hydrodynamic properties in the heave, roll, and pitch motions than in the surge, sway, and yaw motions. The viscous impact on the hydrodynamic properties under the CW condition is larger than that under the HW condition;
3. The means and standard deviations of the motion response, generator power, and mooring line tension are obviously sensitive to the wind and wave directions, but they were insensitive to the viscous effect and current directions under both studied wave conditions. The influence of the viscous effect and current directions on the motion response and generator power mainly shows in the standard deviation rather than in the mean value;
4. Under the CW condition, the generator power is relatively high and stable at  $\theta_w = 120^\circ$  to  $180^\circ$ . Hence,  $\theta_w = 120^\circ$  to  $180^\circ$  is the most favorable wind direction for the studied wind turbine system to operate under the CW condition in the Hsinchu offshore area, where the mean output power can reach 90% of the rated power. The occurrence of the most favorable power performance at  $\theta_w = 120^\circ$  to  $180^\circ$  is clearly explained by the coupled platform motion with the motion-induced and wave-excited components because the center of gravity of the wind turbine system is off its geometrical center. The sums of the means and standard deviations of the mooring line tensions under the CW condition are all smaller than one-seventh of the break load of the mooring line;
5. Under the HW condition, the generator power is relatively high and stable at  $\theta_w = 60^\circ$  to  $180^\circ$ . Hence,  $\theta_w = 60^\circ$  to  $180^\circ$  is the most favorable wind direction for the studied wind turbine system to operate under the HW condition in the Hsinchu offshore area, where the mean output power can reach 95% of the rated power. When compared with the CW results, it is obvious that the increase in the wind speed extends the favorable operation range in the incoming wind direction, as well as enhances the mean output power. The sums of the means and standard deviations of the mooring line tensions under the HW condition are all smaller than one-eighth of the break load of the mooring line;
6. The most favorable wind direction range under the CW and HW conditions in this study is  $\theta_w = 120^\circ$  to  $180^\circ$ , in which the corresponding motion responses all meet the design requirements, and the corresponding power output can reach 90% of the rated power. In the Taiwan Strait, the wind mostly comes from the northeast, with a probability of 40%, followed by the north–northeast, with a probability of 30%. Therefore, the angle between the leading mooring line of the system (i.e., Lines A1 and A2 in the study) and the most possible wind direction, which is the northeast, should be from  $120^\circ$  to  $180^\circ$  in order to deliver a relatively favorable performance.

**Author Contributions:** Conceptualization, H.-Y.T. and S.-W.C.; methodology, H.-Y.T., T.-Y.L. and S.-W.C.; writing—original draft preparation, H.-Y.T.; writing—review and editing, T.-Y.L. and S.-W.C.; visualization, H.-Y.T. and T.-Y.L. All authors have read and agreed to the published version of the manuscript.

**Funding:** This research was funded by the Ministry of Science and Technology, Taiwan, grant numbers MOST 110-3116-F-002-001- and MOST 111-3116-F-002-007.

**Institutional Review Board Statement:** Not applicable.

**Informed Consent Statement:** Not applicable.

**Data Availability Statement:** Not applicable.

**Conflicts of Interest:** The authors declare no conflict of interest.

## Appendix A

### Appendix A.1. Governing Equations

This appendix elaborates the numerical details of the viscous-flow modeling in this study. To obtain the hydrodynamic properties with viscous effects, the load response of the floating body is required, and hence, a forced-motion simulation of the platform with the inclusion of the weight as well as the center of gravity of the wind turbine under a specific frequency was carried out via STAR-CCM+ [43], in which a SIMPLE-type approach was adopted to decouple the velocity and pressure, and a finite volume method of second-order accuracy was employed to discretize the governing equations. The coordinate system for the viscous-flow formulation is shown in Figure A1.

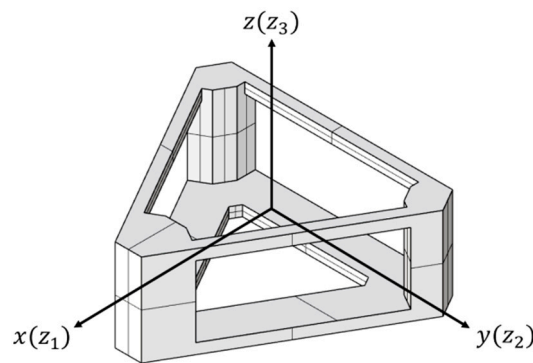


**Figure A1.** Coordinate system for viscous-flow formulation.

Under the assumption of an incompressible fluid, the time-averaged continuity equation is expressed as follows:

$$\frac{\partial u_i}{\partial z_i} = 0, \tag{A1}$$

where the subscripts  $i = 1, 2, 3$  refer to the  $x$ -,  $y$ -, and  $z$ -directions, respectively. The momentum equations are expressed as follows:

$$\frac{\partial \rho u_i}{\partial t} + \frac{\partial (\rho u_i u_j)}{\partial z_j} = -\frac{\partial p}{\partial z_i} + \frac{\partial}{\partial z_i} \left[ \mu \left( \frac{\partial u_i}{\partial z_j} + \frac{\partial u_j}{\partial z_i} \right) \right] - \frac{\partial \overline{\rho u'_i u'_j}}{\partial z_j} + \rho g_i, \tag{A2}$$

where  $u_i$  is the velocity component in the  $z_i$ -direction,  $p$  is the pressure of the fluid,  $\mu$  is the viscosity of the fluid, and  $g_i$  is the gravity component in the  $z_i$ -direction. The third term on the right-hand side of (A2) is the Reynolds stress, which was calculated in this study via an SST  $k$ - $\omega$  model. The key model constants used in the turbulence model are listed in Table A1. The transport equation of the turbulent kinetic energy and its specific dissipation rate are shown below:

$$\frac{\partial (\rho k)}{\partial t} + \frac{\partial (\rho u_j k)}{\partial z_j} = -\beta^* \rho \omega k + \frac{\partial}{\partial z_j} \left[ (\mu + \sigma_k \mu_t) \frac{\partial k}{\partial z_j} \right], \tag{A3}$$

$$\frac{\partial (\rho \omega)}{\partial t} + \frac{\partial (\rho u_j \omega)}{\partial z_j} = -\beta \rho \omega^2 + \frac{\partial}{\partial z_j} \left[ (\mu + \sigma_\omega \mu_t) \frac{\partial \omega}{\partial z_j} \right] + 2(1 - F_1) \frac{\rho \sigma_{\omega 2}}{\omega} \frac{\partial k}{\partial z_j} \frac{\partial \omega}{\partial z_j}. \tag{A4}$$

The employed SST  $k$ - $\omega$  model is a combination of the standard  $k$ - $\omega$  models and standard  $k$ - $\epsilon$  models. The blending function ( $F_1$ ) combines the coefficients of the  $k$ - $\omega$

equation in the boundary layer and the coefficients of the  $k-\epsilon$  equation in the free shear layer and free-flow domain, where  $F_1$  equals unity on a no-slip wall, approaches unity in the boundary layer, and equals zero at the margin of the boundary layer.

**Table A1.** Model constants used in SST  $k-\omega$  model.

Parameter	Value
$F_1$	$\tanh(f_1^4)$
$f_1$	$\min\left[\max\left(\frac{\sqrt{k}}{0.09\omega d}, \frac{500v}{d^2\omega}\right), \frac{2k}{d^2CD_{k\omega}}\right]$
$F_2$	$\tanh(f_2^2)$
$f_2$	$\max\left(\frac{2\sqrt{k}}{\beta^*\omega d}, \frac{500v}{d^2\omega}\right)$
$a_1$	0.31
$\alpha^*$	$F_1 + (1 - F_1)$
$\beta$	$0.075F_1 + 0.0828(1 - F_1)$
$\beta^*$	$0.09F_1 + 0.09(1 - F_1)$
$\sigma_k$	$0.85F_1 + 1(1 - F_1)$
$\sigma_\omega$	$0.5F_1 + 0.856(1 - F_1)$
$\mu_t$	$\min\left\{\frac{1}{\max(\omega/\alpha^*, \left[\frac{ \nabla\bar{v}-\nabla\bar{v}^T }{2}\right]F_2/a_1)}, \frac{0.6}{\sqrt{3S}}\right\}$
$CD_{k\omega}$	$\max\left(\frac{1}{\omega} \nabla k \cdot \nabla \omega, 10^{-20}\right)$

The volume of fluid (VOF) method was used for the simulation of the free-surface flow [44]. When multiple fluids are present in a cell, the volume fraction of the  $i$ -th fluid is expressed as follows:

$$\alpha_i = \frac{V_i}{V}, \tag{A5}$$

where  $V_i$  is the volume occupied by the  $i$ -th fluid in a cell, and  $V$  is the cell volume. Therefore, the volume fraction of all the fluids in each cell must satisfy the following formula:

$$\sum_{i=1}^N \alpha_i = 1, \tag{A6}$$

where  $N$  is the number of fluids. When  $\alpha_i = 0$ , this means that there is no  $i$ -th fluid present in the cell. When  $\alpha_i = 1$ , this means that only the  $i$ -th fluid occupies the cell. When  $0 < \alpha_i < 1$ , this means that there are other fluids in addition to the  $i$ -th fluid coexisting in the cell, and a free surface is implied in the cell. As a result, the density ( $\rho$ ) and viscosity ( $\mu$ ) in a cell are the weighted density and viscosity averages of all the fluid present in the cell, respectively:

$$\rho = \sum_{i=1}^N \rho_i \alpha_i, \tag{A7}$$

$$\mu = \sum_{i=1}^N \mu_i \alpha_i, \tag{A8}$$

where  $\rho_i$  and  $\mu_i$  are the density and viscosity of the  $i$ -th fluid, respectively. The continuity equation of the  $i$ -th fluid is formulated as follows:

$$\frac{\partial \alpha_i}{\partial t} + u_k \frac{\partial \alpha_i}{\partial z_k} + \nabla \cdot (\alpha_i \mathbf{v}_{d,i}) + \nabla \cdot [\alpha_i (1 - \alpha_i) \mathbf{v}_{c,i}] = 0, \tag{A9}$$

where  $\mathbf{v}_{d,i}$  and  $\mathbf{v}_{c,i}$  are the diffusion velocity and boundary-sharpening velocity of the  $i$ -th fluid, respectively, which are defined as follows:

$$\mathbf{v}_{c,i} = C_\alpha |\mathbf{v}| \frac{\nabla \alpha_i}{|\nabla \alpha_i|}, \tag{A10}$$

where  $C_\alpha$  is the sharpening factor, and  $\mathbf{v}$  is the velocity vector. Based on the normalized variable diagram, the normalized volume fraction value at the cell interface between the central cell and downwind cell ( $\zeta_f$ ) is defined in (A11) and Figure A2, where  $\mathbf{a}$  is the area vector of the cell interface, and  $\mathbf{n}$  is the normal vector of the fluid interface.

$$\zeta_f = \begin{cases} \zeta_c & \text{for } \zeta_c \notin [0, 1] \\ 2\zeta_c & \text{for } \zeta_c \in [0, 0.5], \\ 1 & \text{for } \zeta_c \in [0.5, 1] \end{cases} \tag{A11}$$

where the normalized volume fraction of the central cell ( $\zeta_c$ ) is defined as follows:

$$\zeta_c = \frac{\alpha_c - \alpha_u}{\alpha_d - \alpha_u}, \tag{A12}$$

where  $\alpha_u$ ,  $\alpha_c$ , and  $\alpha_d$  are the volume fraction of the upwind, central, and downwind cells, respectively.  $\zeta_f$  is further modified to  $\zeta_f^*$  via the Courant number ( $Co$ ):

$$\zeta_f^* = \begin{cases} \zeta_f & \text{for } Co < Co_l \\ \zeta_c + (\zeta_f - \zeta_c) \frac{Co_u - Co}{Co_u - Co_l} & \text{for } Co_l \leq Co < Co_u, \\ \zeta_c & \text{for } Co_u \leq Co \end{cases} \tag{A13}$$

where the upper bound of the Courant number ( $Co_u$ ) is unity, and the lower bound of the Courant number ( $Co_l$ ) is 0.5. The Courant number ( $Co$ ) is defined as follows:

$$Co = \frac{\mathbf{v} \cdot \mathbf{a}}{V_c} \delta t, \tag{A14}$$

where  $V_c$  is the characteristic velocity, and  $\delta t$  is the time-step size. When  $Co < Co_l$ , (A11) is used. When  $Co_l \leq Co < Co_u$ , (A11) and the first-order upwind method are used. When  $Co_u \leq Co$ , the first-order upwind method is used. The variable  $\zeta_f^*$  is further modified to  $\zeta_f^{**}$  via the angle between the fluid interface and cell interface ( $\theta_p$ ):

$$\zeta_f^{**} = \zeta_f^* (\cos \theta_p)^{C_\theta} + \zeta_c (1 - (\cos \theta_p)^{C_\theta}), \tag{A15}$$

where the angle factor ( $C_\theta$ ) is set to 0.05. The volume fraction ( $\alpha_f$ ) at the cell interface is then obtained from the equation below:

$$\alpha_f = \zeta_f^{**} (\alpha_d - \alpha_u) + \alpha_u. \tag{A16}$$

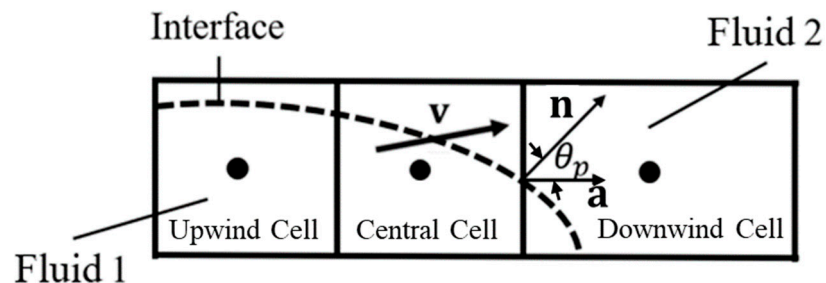


Figure A2. Schematic of fluid interface and cells.

Appendix A.2. Setup of Modeling

The platform undergoes a forced motion, and the velocity of the forced motion is given as follows:

$$V_f = \zeta \omega \sin(\omega t), \tag{A17}$$

where  $V_f$  is the generalized velocity of the motion,  $\omega$  is the angular frequency of the motion, and  $\zeta$  is the generalized amplitude of the motion, which was assumed to be 1 m for translation and  $1^\circ$  for rotation in this study. Generally, at least ten motion periods are calculated in the numerical simulation, in which the typical  $y^+$  ranges between 50 and 100.

Overset mesh was used to simulate the forced motion of the floating platform in this study. Compared with the dynamic mesh approach, which is prone to result in a negative volume of cells, the overset mesh is relatively simple to use to define computation grids, and it easily maintains its fine mesh quality during the body movement. The complete mesh is composed of background and platform meshes. The former is defined with the whole computational domain, while the latter is defined with the overset domain. The entire component mesh is forced to translate or rotate during the forced-motion simulation. The boundary condition of the platform surface is a no-slip wall. The boundary condition of the lower boundary of the computational domain is assumed to be a no-slip wall, and the other boundaries use a zero-velocity condition due to the far-field assumption in which the initial velocity of the flow field is set to zero.

The upper and lower boundaries of the computational domain were located 70 m above and below the water surface because 70 m is the typical water depth of the Hsinchu offshore area. The height of the overset boundary was 80 m, which is close to the characteristic length ( $L$ ) of the Taida platform. The length of the computational domain and overset domain is proportional to the wavelength ( $\lambda$ ), which is estimated by the shallow-water equation:

$$\lambda = \frac{gT^2}{2\pi} \tag{A18}$$

where  $T$  denotes the period of motion. The computational domain has a length of  $20\lambda$ , and the overset domain has a length of  $3\lambda$ . For the two wave conditions (i.e., the common wave (CW) condition and high wave (HW) condition), the corresponding zero-crossing periods were 5.5 s and 7.5 s, respectively. Following (A18), the corresponding wave lengths were 48 m and 92 m, respectively. Therefore, the lengths of the computational domain and overset domain of the CW condition were 960 m and 144 m, respectively, and those of the HW condition were 1840 m and 276 m, respectively. The dimensions and boundary conditions of the computational domain are shown in Figure A3.

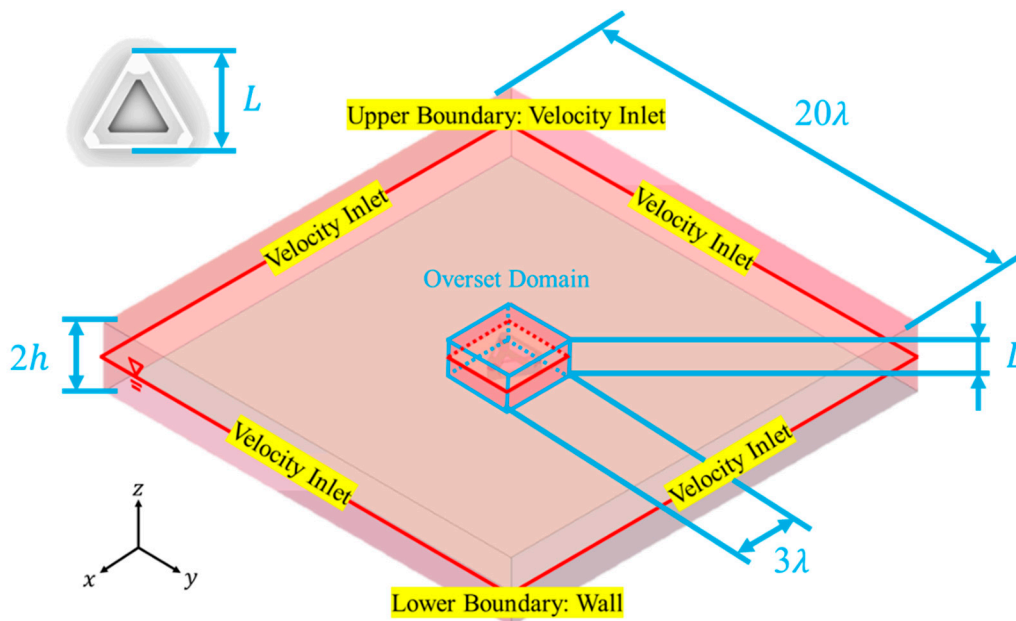


Figure A3. Computational domain of viscous-flow modeling.

Appendix A.3. Setup of Mesh

The parameters of the mesh generation are shown in Table A2, and the numerical mesh is depicted in Figure A4. The vertical cut of the numerical mesh at  $y = 0$  is illustrated in Figure A4a, where the platform mesh is embedded inside the background mesh. Table A2a discloses the cell size alongside the mesh number employed in the forced-motion simulation. The background mesh refinement setup is shown in Table A2b. The background mesh was refined with three grid levels to better resolve the flow near the platform (Figure A4b). This successive mesh refinement was only performed on the  $xy$  plane. To accurately capture the free-surface evolution, the cell size at the free surface needs to be refined in the  $z$ -direction. As shown in Figure A4c,d, the refinement region of the platform mesh must be thicker than that of the background mesh, and especially in the heave, roll, and pitch motions due to the displacement of the platform mesh in the  $z$ -direction. Moreover, the peripheral part of the background mesh needs to be further refined to capture the free-surface variation due to the rapid decay of the outgoing waves. The mesh refinement setup near the free surface is shown in Table A2c.

**Table A2.** Mesh parameters of viscous-flow modeling: (a) mesh number and cell size; (b) background mesh refinement setup; (c) mesh refinement setup at free surface.

(a)			
Properties (Unit)		CW Condition	HW Condition
Platform Surface Mesh Faces	Surge, Sway, Yaw	$2.799 \times 10^5$	$2.793 \times 10^5$
	Heave, Roll, Pitch	$6.459 \times 10^5$	$5.937 \times 10^5$
Total Cell Numbers	Surge, Sway, Yaw	$3.413 \times 10^6$	$4.230 \times 10^6$
	Heave, Roll, Pitch	$7.559 \times 10^6$	$8.096 \times 10^6$
Platform Surface Mesh Size (m)			0.625
Platform Mesh Cell Size (m)			6.25
Maximum Background Mesh Cell Size (m)			50
(b)			
Outer Boundary Shape	Outer Boundary of Refinement Region on $xy$ -Plane from Origin	Cell Size Scale	
Cylinder	$> 7\lambda$	1	
	$7\lambda$	1/2	
	$5\lambda$	1/4	
	$3\lambda$	1/8	
(c)			
Properties (Unit)		CW Condition	HW Condition
Region Thickness of Platform	Surge, Sway, Yaw	4	4
Mesh Refinement (m)	Heave, Roll, Pitch	11	10
Region Thickness of Background Mesh Refinement (m)		2	2
Outer Boundary of Inner Refinement Region on $xy$ -Plane		Circle with Radius of $5\lambda$ at Origin	
Cell Size in $z$ -Direction (m)	Inner Region	0.05	
	Outer Region	0.025	

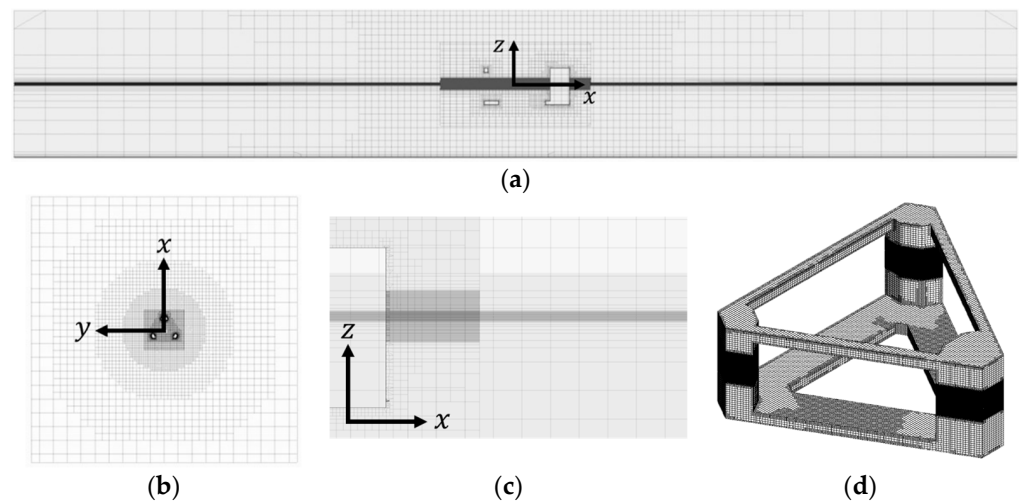


**Figure A4.** Mesh of viscous-flow modeling: (a) vertical cut at  $y = 0$ ; (b) horizontal cut at  $z = 0$ ; (c) zoomed view of horizontal cut at  $y = 0$ ; (d) surface mesh of platform.

## References

1. Global Wind Energy Council. Global Wind Report 2022. 2022. Available online: <https://gwec.net/global-wind-report-2022/> (accessed on 22 August 2022).
2. Open Access News. 2022. Offshore Wind Energy in Taiwan. Available online: <https://www.openaccessgovernment.org/taiwan-offshore-wind/129010/> (accessed on 22 August 2022).
3. *Wind Resource Assessment Handbook*. NREL/TAT-5-15283-01; National Renewable Energy Laboratory: Golden, CO, USA, 2011.
4. Wang, Y.K.; Chai, J.F.; Chang, Y.W.; Huang, T.Y.; Kuo, Y.S. Development of Seismic Demand for Chang-Bin Offshore Wind Farm in Taiwan Strait. *Energies* **2016**, *9*, 1036. [CrossRef]
5. Chang, T.J.; Chen, C.L.; Tu, Y.L.; Yeh, H.T.; Wu, Y.T. Evaluation of the Climate Change Impact on Wind Resources in Taiwan Strait. *Energy Convers. Manag.* **2015**, *95*, 435–445. [CrossRef]
6. Uzunoglu, E.; Soares, C.G. Hydrodynamic design of a free-float capable tension leg platform for a 10 MW wind turbine. *Ocean. Eng.* **2020**, *197*, 106888. [CrossRef]
7. Lee, Y.J.; Ho, C.Y.; Huang, Z.Z.; Wang, Y.C. Improvements on the Output of a Spar-Type Floating Wind Turbine Influenced by Wave-Induced Oscillation. *J. Taiwan Soc. Nav. Archit. Mar. Eng.* **2015**, *34*, 55–62.
8. Huang, Z.Z. Dynamic Response of Floating Offshore Wind Turbine. Ph.D. Thesis, Department of Engineering Science and Ocean Engineering, National Taiwan University, Taipei, Taiwan, 2013.
9. Wang, Y.C. Motion Characteristics and Power Evaluation on Floating Offshore Wind Turbine. Ph.D. Thesis, Department of Engineering Science and Ocean Engineering, National Taiwan University, Taipei, Taiwan, 2011.
10. Chen, C.Y. Comparative Study on Semi-Submersible Floating Platforms for Offshore Wind in Taiwan Strait. Master's Thesis, Department of Engineering Science and Ocean Engineering, National Taiwan University, Taipei, Taiwan, 2020.
11. Hong, J.J. Performance Prediction of a Disk-Type Semi-Submersible Floating Platform in Taiwan Strait. Ph.D. Thesis, Department of Engineering Science and Ocean Engineering, National Taiwan University, Taipei, Taiwan, 2022.
12. Li, B.; Liu, K.; Yan, G.; Ou, J. Hydrodynamic Comparison of a Semi-Submersible, TLP, and Spar: Numerical Study in the South China Sea Environment. *J. Mar. Sci. Appl.* **2011**, *10*, 306–314. [CrossRef]
13. De Guzman, S.; Maron, D.; Bueno, P.; Taboada, M. A Reduced Draft Spar Concept for Large Offshore Wind Turbines. In Proceedings of the 37th International Conference on Ocean, Offshore and Arctic Engineering, Madrid, Spain, 17–22 June 2018; American Society of Mechanical Engineers: New York, NY, USA, 2018.
14. Quest Floating Wind Energy. 2022. Available online: <https://questfwe.com> (accessed on 22 August 2022).
15. Jonkman, J.; Butterfield, S.; Musial, W.; Scott, G. *Definition of a 5-MW Reference Wind Turbine for Offshore System Development*. NREL/TP-500-38060; National Renewable Energy Laboratory: Golden, CO, USA, 2009.
16. Bak, C.; Zahle, F.; Bitsche, R.; Kim, T.; Yde, A.; Henriksen, L.C.; Hansen, M.H.; Blasques, J.P.A.A.; Gaunaa, M.; Natarajan, A. The DTU 10-MW Reference Wind Turbine. In Proceedings of the Danish Wind Power Research, Fredericia, Denmark, 27–28 May 2013.
17. Liu, J.; Manuel, L. Alternative Mooring Systems for a Very Large Offshore Wind Turbine Supported by a Semisubmersible Floating Platform. *J. Sol. Energy Eng.* **2018**, *140*, 051003. [CrossRef]
18. Gaertner, E.; Rinker, J.; Sethuraman, L.; Zahle, F.; Anderson, B.; Barter, G.; Abbas, N.; Meng, F.; Bortolotti, P.; Skrzypinski, W.; et al. *Definition of the IEA Wind 15-Megawatt Offshore Reference Wind Turbine*; NREL/TP-5000-75698; National Renewable Energy Laboratory: Golden, CO, USA, 2020.
19. Udoh, I.E.; Zou, J. Driving Down Cost: A Case Study of Floating Substructure for A 10MW Wind Turbine. In *Offshore Technology Conference*; OnePetro: Richardson, TX, USA, 2019.

20. Zhang, Y.; Kim, B. A Fully Coupled Computational Fluid Dynamics Method for Analysis of Semi-Submersible Floating Offshore Wind Turbines Under Wind-Wave Excitation Conditions Based on OC5 Data. *Appl. Sci.* **2018**, *8*, 2314. [CrossRef]
21. Tran, T.T.; Kim, D.H. Fully coupled aero-hydrodynamic analysis of a semi-submersible FOWT using a dynamic fluid body interaction approach. *Renew. Energy* **2016**, *92*, 244–261. [CrossRef]
22. Robertson, A.; Jonkman, J.; Vorpahl, F.; Popko, W.; Qvist, J.; Froyd, L.; Chen, X.; Azcona, J.; Uzungoglu, E.; Guedes Soares, C. *Offshore Code Comparison Collaboration, Continuation within IEA Wind Task 30: Phase II Results Regarding a Floating Semisubmersible wind System*; National Renewable Energy Lab.: Golden, CO, USA, 2014.
23. Luquet, R.; Ducrozet, G.; Gentaz, L.; Ferrant, P.; Alessandrini, B. Applications of the SWENSE method to seakeeping simulations in irregular waves. In Proceedings of the 9th International Conference on Numerical Ship Hydrodynamics, Ann Arbor, MI, USA, 5–8 August 2007.
24. Sethuraman, L.; Venugopal, V. Hydrodynamic response of a stepped-spar floating wind turbine: Numerical modelling and tank testing. *Renew. Energy* **2013**, *52*, 160–174. [CrossRef]
25. Antonutti, R.; Peyrard, C.; Johanning, L.; Incecik, A.; Ingram, D. An investigation of the effects of wind-induced inclination on floating wind turbine dynamics: Heave plate excursion. *Ocean. Eng.* **2014**, *91*, 208–217. [CrossRef]
26. Nematbakhsh, A.; Olinger, D.J.; Tryggvason, G. Nonlinear simulation of a spar buoy floating wind turbine under extreme ocean conditions. *J. Renew. Sustain. Energy* **2014**, *6*, 033121. [CrossRef]
27. Liu, Y.; Peng, Y.; Wan, D. Numerical Investigation on Interaction between a Semi-Submersible Platform and its Mooring System. In *International Conference on Offshore Mechanics and Arctic Engineering*; American Society of Mechanical Engineers: New York, NY, USA, 2015; p. 56550.
28. Karimirad, M.; Michailides, C. V-shaped semisubmersible offshore wind turbine: An alternative concept for offshore wind technology. *Renew. Energy* **2015**, *83*, 126–143. [CrossRef]
29. Zheng, X.Y.; Lei, Y. Stochastic response analysis for a floating offshore wind turbine integrated with a steel fish farming cage. *Appl. Sci.* **2018**, *8*, 1229. [CrossRef]
30. Ishihara, T.; Zhang, S. Prediction of dynamic response of semi-submersible floating offshore wind turbine using augmented Morison's equation with frequency dependent hydrodynamic coefficients. *Renew. Energy* **2019**, *131*, 1186–1207. [CrossRef]
31. Lerch, M.; De-Prada-Gil, M.; Molins, C. The influence of different wind and wave conditions on the energy yield and downtime of a spar-buoy floating wind turbine. *Renew. Energy* **2019**, *136*, 1–14. [CrossRef]
32. Zhang, P.; Yang, S.; Li, Y.; Gu, J.; Hu, Z.; Zhang, R.; Tang, Y. Dynamic response of articulated offshore wind turbines under different water depths. *Energies* **2020**, *13*, 2784. [CrossRef]
33. Ferrandis, J.D.Á.; Bonfiglio, L.; Rodríguez, R.Z.; Chryssostomidis, C.; Faltinsen, O.M.; Triantafyllou, M. Influence of viscosity and non-linearities in predicting motions of a wind energy offshore platform in regular waves. *J. Offshore Mech. Arct. Eng.* **2020**, *142*, 062003. [CrossRef]
34. Hsu, I.J.; Ivanov, G.; Ma, K.T.; Huang, Z.Z.; Wu, H.T.; Huang, Y.T.; Chou, M. Optimization of Semi-Submersible Hull Design for Floating Offshore Wind Turbines. In Proceedings of the ASME 2022 41st International Conference on Ocean, Offshore and Arctic Engineering, Hamburg, Germany, 5–10 June 2022.
35. Huang, W.H. Influence of Water Depth Variation on the Mooring Line Design for FOWT in Shallow Waters. Master's Thesis, Department of Hydraulic and Ocean Engineering, National Cheng Kung University, Tainan, Taiwan, 2021.
36. DNV GL. *DNVGL-RP-0286 Coupled Analysis of Floating Wind Turbines*; DNV GL: Oslo, Norway, 2019.
37. Ikhennicheu, M.; Lynch, M.; Doole, S.; Borisade, F.; Matha, D.; Dominguez, J.L.; Vicente, R.D.; Habekost, T.; Ramirez, L.; Potestio, S.; et al. D2.1 Review of the State of the Art of Mooring and Anchoring Designs, Technical Challenges and Identification of Relevant DLCs. Technical Report. CoreWind Project. 2020. Available online: <https://corewind.eu/wp-content/uploads/files/publications/COREWIND-D2.1-Review-of-the-state-of-the-art-of-mooring-and-anchoring-designs.pdf> (accessed on 22 August 2022). Technical Report. CoreWind Project.
38. Gaertner, E.; Rinker, J.; Sethuraman, L.; Zahle, F.; Anderson, B.; Barter, G.; Abbas, N.; Meng, F.; Bortolotti, P.; Skrzypinski, W.; et al. 15MW Reference Wind Turbine Repository Developed in Conjunction with IEA Wind. 2022. Available online: <https://github.com/IEAWindTask37/IEA-15--240-RWT/> (accessed on 22 August 2022).
39. Chuang, T.C.; Yang, W.H.; Yang, R.Y. Experimental and Numerical Study of a Barge-Type FOWT Platform under Wind and Wave Load. *Ocean. Eng.* **2021**, *230*, 109015. [CrossRef]
40. Jonkman, J.; Jason, M.L.; Marchall, B., Jr. *FAST User's Guide*; National Renewable Energy Lab: Golden, CO, USA, 2005.
41. Wehausen, J.V.; Laitone, E.V. Surface Waves in Fluid Dynamics III. In *Handbuch der Physik*; Springer Verlag: Berlin, Germany, 1960; Volume 9, pp. 446–778.
42. Orcina. *OrcaFlex Documentation Version 11.2d*; Orcina: Ulverston, UK, 2022.
43. Siemens. *Simcenter STAR-CCM+ User Guide Version 2020.1*; Siemens: Munich, Germany, 2020.
44. Hirt, C.W.; Nichols, B.D. Volume of Fluid Method for the Dynamics of Free Surface. *J. Comput. Phys.* **1981**, *39*, 201–225. [CrossRef]

**Disclaimer/Publisher's Note:** The statements, opinions and data contained in all publications are solely those of the individual author(s) and contributor(s) and not of MDPI and/or the editor(s). MDPI and/or the editor(s) disclaim responsibility for any injury to people or property resulting from any ideas, methods, instructions or products referred to in the content.